Space–Time Spectral Analysis of the Moist Static Energy Budget Equation

KAZUAKI YASUNAGA

Department of Earth Science, Graduate School of Science and Engineering, University of Toyama, Toyama, Japan

SATORU YOKOI

Japan Agency for Marine-Earth Science and Technology, Yokosuka, Japan

KUNIAKI INOUE

NOAA/Geophysical Fluid Dynamics Laboratory, Princeton, New Jersey, and University Corporation for Atmospheric Research, Boulder, Colorado

BRIAN E. MAPES

Rosenstiel School of Marine and Atmospheric Science, University of Miami, Coral Gables, Florida

(Manuscript received 29 May 2018, in final form 18 October 2018)

ABSTRACT

The budget of column-integrated moist static energy (MSE) is examined in wavenumber–frequency transforms of longitude–time sections over the tropical belt. Cross-spectra with satellite-derived precipitation (TRMM-3B42) are used to emphasize precipitation-coherent signals in reanalysis [ERA-Interim (ERAI)] estimates of each term in the budget equation. Results reveal different budget balances in convectively coupled equatorial waves (CCEWs) as well as in the Madden–Julian oscillation (MJO) and tropical depression (TD)-type disturbances. The real component (expressing amplification or damping of amplitude) for horizontal advection is modest for most wave types but substantially damps the MJO. Its imaginary component is hugely positive (it acts to advance phase) in TD-type disturbances and is positive for MJO and equatorial Rossby (ERn1) wave disturbances (almost negligible for the other CCEWs). The real component of vertical advection is negatively correlated (damping effect) with precipitation with a magnitude of approximately 10% of total latent heat release for all disturbances except for TD-type disturbance. This effect is overestimated by a factor of 2 or more if advection is computed using the time–zonal mean MSE, suggesting that nonlinear correlations between ascent and humidity would be positive (amplification effect). ERAI-estimated radiative heating has a positive real part, reinforcing precipitation-correlated MSE excursions. The magnitude is up to 14% of latent heating for the MJO and much less for other waves. ERAI-estimated surface flux has a small effect but acts to amplify MJO and ERn1 waves. The imaginary component of budget residuals is large and systematically positive, suggesting that the reanalysis model's physical MSE sources would not act to propagate the precipitation-associated MSE anomalies properly.

1. Introduction

The budget equation of column-integrated water vapor [WV (CWV)] and column-integrated dry static energy [DSE (CDSE)] read

$$\left\langle \frac{\partial q}{\partial t} \right\rangle = -\langle \mathbf{v}_h \cdot \nabla_h q \rangle - \left\langle \omega \frac{\partial q}{\partial p} \right\rangle + E - P, \quad \text{and} \tag{1}$$

$$\left\langle \frac{\partial s}{\partial t} \right\rangle = -\langle \mathbf{v}_h \cdot \nabla_h s \rangle - \left\langle \omega \frac{\partial s}{\partial p} \right\rangle + \langle Q_R \rangle + H + LP, \tag{2}$$

where q is specific humidity, $\mathbf{v}_h$ is the horizontal wind vector, ω is vertical pressure velocity, E is surface evaporation, P is surface precipitation, s is dry static energy, H is sensible heat flux from the surface, Q_R is net radiative heating rate, and angle brackets indicate

Denotes content that is immediately available upon publication as open access.

Corresponding author: Kazuaki Yasunaga, yasunaga@sus.u-toyama.ac.jp

DOI: 10.1175/JCLI-D-18-0334.1

mass-weighted column integration. By combining Eqs. (1) and (2), the budget equation of the column-integrated moist static energy [MSE (CMSE)] is obtained,

$$\left\langle \frac{\partial m}{\partial t} \right\rangle = -\langle \mathbf{v}_h \cdot \nabla_h m \rangle - \left\langle \omega \frac{\partial m}{\partial p} \right\rangle + \langle Q_R \rangle + (H + LE), \tag{3}$$

where m is moist static energy, with L the latent heat of vaporization.

A horizontal-scale separation is implied when $\mathbf{v}_h$ and ω in the advection terms are interpreted as large-scale motions averaged over an area containing a cloud ensemble, as described in Yanai et al. (1973). Therefore, when we estimate advection terms in Eq. (3) using such scale-filtered reanalysis data, subfilter eddy flux convergence terms appear on the right-hand side (RHS). Following custom, we assume that cloud-scale (subfilter scale) horizontal wind perturbations have no significant correlations with moisture and temperature perturbations and neglect the horizontal eddy terms, while the convergence of vertical subfilter eddy flux reduces to the surface molecular flux ($H + LE$) in the column integral.

In the tropical troposphere, temperature gradients are small because of the large Rossby radius of deformation (Charney 1963), reflecting the mighty power of gravity to flatten density surfaces efficiently as diabatic effects act more gently to deform them. Temporal changes of temperature are negligible as well, and this combination is referred to as the weak temperature gradient (WTG) approximation (Sobel et al. 2001). Under the WTG approximation, the evolution of CMSE prognosed by Eq. (3) is L times the evolution of CWV or ''precipitable'' water. The complex details of error-prone precipitation estimation are side stepped in constructing Eq. (3), in remarkable contrast to Eqs. (1) and (2) where they are first order, balanced by corresponding P-proportional details in the vertical advection fields. As a result, even though $\langle \omega \partial m/\partial p \rangle$ does not formally vanish like P, it is much more tractable and well behaved than $\langle \omega \partial q/\partial p \rangle$ and $\langle \omega \partial s/\partial p \rangle$ in Eqs. (1) and (2), which defy direct observational estimation.

The response to localized heating (like a water-condensation event) in the stratified tropical atmosphere is not confined within the local area near the precipitation, but is extended to a much wider area through the mechanism of equatorial internal waves (Matsuno 1966; Itoh 1977; Gill 1980). The larger-scale motions associated with such waves, in turn, advect water vapor and DSE through Eqs. (1) and (2) in ways that affect the probability of subsequent convection-mediated precipitation. The interplay of these mechanisms makes precipitating convectively coupled tropical disturbances fascinating and challenging to understand and predict.

Unfortunately, Eqs. (1) and (2) are unsatisfactory to work with directly because of the aforementioned large but intimately cancelling terms in the spotty fields of P and vertical advection. Data-based estimation and summation of those two terms individually are far less reliable than the holistic principle of WTG (and the related boundedness of q). The CMSE budget Eq. (3) provides an ansatz: a clever tactic within a larger strategy of understanding precipitation variability. Since knowing CMSE variations is tantamount to knowing CWV variations under the WTG approximation, and since the expectation value of precipitation is monotonically (albeit nonlinearly) dependent on CWV (e.g., Bretherton et al. 2004; Neelin et al. 2009; Schiro et al. 2016; Mapes et al. 2018; Rushley et al. 2018), precipitation in tropical disturbances can be constrained meaningfully and rigorously (if somewhat obliquely, incompletely, and nonuniquely) through this clever use of the much more tractable Eq. (3). Strategically, this approach is perhaps akin to formally neglecting ageostrophic winds in quasigeostrophic (QG) theory, in order to then estimate vertical wind (or horizontal wind divergence), which is ageostrophic. The roundabout quality of such ''precipitation budget'' tactics is discussed in Adames (2017), for instance.

In this way, prior studies of the CMSE budget equation have illuminated aspects of many moist tropical weather phenomena, including convectively coupled equatorial wave (CCEW) disturbances (Kiladis et al. 2009) and the Madden–Julian oscillation (MJO; Madden and Julian 1971, 1972). For instance, Kiranmayi and Maloney (2011) examined MSE budgets of the MJO and found significant contributions from horizontal advection in increasing (decreasing) column MSE before (after) peak MJO convection. Sobel et al. (2014) analyzed CMSE over the tropical Indian Ocean and found that radiative feedbacks importantly enhance the MJO's moist static energy anomalies, while its eastward propagation is associated with advection of MSE. Similar results were also reported over the eastern part of the Maritime Continent by Yokoi and Sobel (2015). Inoue and Back (2015a) explored MSE budgets in rawinsonde array time series data over the western Pacific and found significantly different term balances on different time scales: For higher-frequency variations, vertical advection predominates in explaining CMSE variations, while horizontal advection and physical source terms contribute more to longer time-scale variations. In apparent contrast, studies by Masunaga and L'Ecuyer (2014) and Sumi and Masunaga (2016) emphasized the

importance of horizontal as well as vertical MSE advection in budgets of their shorter-time-scale CMSE variations. The overarching point is that the relative sizes of the CMSE budget's terms are space- and time-scale dependent.

Other CMSE budget investigations have used lagged regression or composite analysis, often with base time series from filtered precipitation data, with signals isolated by masking precipitation variance in the wavenumber–frequency domain and transforming back to physical space (e.g., Kiladis and Weickmann 1992; Bantzer and Wallace 1996; Wheeler et al. 2000; Yasunaga and Mapes 2012). The wavenumber–frequency masking regions (filter boxes) for CCEW anomalies are somewhat ad hoc, but a fairly customary set has evolved through a wide variety of uses in previous investigations and will be utilized later in this study.

In an attempt to synthesize these insights from phenomenon-specific and frequency-specific studies, this study extends CMSE budget analysis to the entire space–time spectral domain for the tropical belt. We isolate precipitation-associated and well-analyzed MSE fluctuations by utilizing cross-spectra between reanalysis-derived estimates of each term in the CMSE budget equation and nearly independently estimated satellite-derived precipitation. From that full-spectral-domain result, we can summarize the results in tables for the entire customary set of filter boxes encompassing the whole family of tropical disturbances. In this way, other CMSE budget studies can at least be emplaced within a common reference standard, even if our present datasets are not definitively accurate—as our analysis of residuals below indicates they are not.

2. Data and methodology

a. Data description

For precipitation estimates, TRMM-3B42, version 7, data are used, spanning the period from 1 January 1998 to 31 December 2013 (Huffman et al. 2007). For dynamical and physical fields, including horizontal and vertical winds, geopotential height, temperature, and specific humidity, our work uses European Centre for Medium-Range Weather Forecasts (ECMWF) interim reanalysis (ERA-Interim, herein ERAI) data (Berrisford et al. 2011). Short-term (6 and 12 h) forecast values from the ERAI dataset were used for model physics scheme–derived source terms such as the latent and sensible heat fluxes at the surface and net radiation at the surface and top of atmosphere. To derive the CMSE budget terms in Eq. (3), vertical integrations were calculated from the surface to 100 hPa. Strictly speaking, the vertically integrated radiative heating rate was calculated as the difference in the radiative flux between the surface and top of the atmosphere fields. In part because of this discrepancy, but also because of other ERAI field and process errors, the data-estimated CMSE budget equation contains residuals, which will be discussed in section 5.

b. Calculation procedure

Space–time power and cross-power spectra were calculated using a standard fast Fourier transform (FFT) algorithm. The calculation procedure is identical to our previous paper (Yasunaga and Mapes 2012) and will be briefly repeated here.

First, precipitation data and estimates of each term in Eq. (3) were partitioned into equatorially symmetric and antisymmetric components for the equatorial band 15°S–15°N. Then, the mean and first three harmonics of the climatological annual cycle were subtracted to yield temporal anomalies. Time series of those anomaly data were divided into 92-day segments, allowing overlaps of about two months to prevent information losses due to windowing of segments. Each segment was detrended and tapered to zero over the first and last nine days. Finally, the power and cross-spectra were computed for each segment and averaged over all segments.

To facilitate visualization and increase degrees of freedom (DOFs), 1–2–1 smoothing in frequency and wavenumber direction were applied. The DOF for statistical significance testing can be estimated as

$$\mathrm{DOF} = \frac{2(\text{amplitude and phase}) \times 16(\text{years}) \times 365(\text{days yr}^{-1}) \times 2(\text{for 1–2–1 filter in frequency}) \times 2(\text{for 1–2–1 filter in wavenumber})}{92(\text{days segment}^{-1})} \approx 507.$$

The number might be debatable within a factor of 2, but undersampling is not the largest caveat or uncertainty of any result emphasized here.

c. *Cross-spectra of column-integrated budget equation of MSE*

Through the discrete space–time Fourier transforms of two fields (A and B), a set of complex numbers are obtained for the discrete zonal wavenumbers k and frequencies ω, which is denoted as $A_{k,\omega}$ and $B_{k,\omega}$. The power (C_{AA} and C_{BB}) and cross-power (C_{AB}) spectra are expressed as

$$C_{AA} = A^*_{k,\omega}A_{k,\omega} = |A_{k,\omega}|^2, C_{BB} = B^*_{k,\omega}B_{k,\omega} = |B_{k,\omega}|^2,$$
$$C_{AB} = A^*_{k,\omega}B_{k,\omega},$$

where $A^*_{k,\omega}$ and $B^*_{k,\omega}$ indicate a complex conjugate of $A_{k,\omega}$ and $B_{k,\omega}$, respectively. Although the power spectrum is real, the cross-spectrum is a complex number. The real and imaginary components are referred to as the cospectrum and quadrature spectrum, respectively. The coherency between the two variables can be measured by normalizing the squared magnitude of cross-spectrum with the power of the individual fields, which is referred to the coherence squared spectrum (coh^2),

$$\mathrm{coh}^2 = \frac{|\overline{A^*_{k,\omega}B_{k,\omega}}|^2}{\overline{A^*_{k,\omega}A_{k,\omega}} \times \overline{B^*_{k,\omega}B_{k,\omega}}},$$

where the overbar indicates an average over realizations, since the coherence squared is identically 1 for each discrete frequency without any averaging procedure. In the present analysis, the power and cross-spectra are computed for each time series segment, and those are averaged over all the segments, applying the 1–2–1 filter in frequency and wavenumber direction. The mean phase relationship of the two coherent variables can also be measured by the ratio of cospectrum and quadrature spectrum. Numerous studies on tropical moist disturbances have used the cross-power spectrum: Hayashi (1974), Wheeler and Kiladis (1999), Hendon and Wheeler (2008), Yasunaga and Mapes (2012, 2014), and more.

Since the Fourier transform is a linear operation, the column-integrated budget equation of MSE holds after transforming to spectral space. That is, Eq. (3) becomes

$$\left\langle \frac{\partial m}{\partial t} \right\rangle_{k,\omega} = -\langle \mathbf{v}_h \cdot \nabla_h m \rangle_{k,\omega} - \left\langle \omega \frac{\partial m}{\partial p} \right\rangle_{k,\omega} + \langle Q_R \rangle_{k,\omega} + (H + LE)_{k,\omega},$$

with a residual term implied on the right when the terms of this physical law are estimated separately from imperfect data. The cross-power spectrum between the precipitation and each term in the MSE budget equation is obtained by transforming precipitation P into spectral (k, ω) space and multiplying its complex conjugate by the above equation:

$$P^*_{k,\omega}\left\langle \frac{\partial m}{\partial t} \right\rangle_{k,\omega} = -P^*_{k,\omega}\langle \mathbf{v}_h \cdot \nabla_h m \rangle_{k,\omega} - P^*_{k,\omega}\left\langle \omega \frac{\partial m}{\partial p} \right\rangle_{k,\omega} + P^*_{k,\omega}\langle Q_R \rangle_{k,\omega} + P^*_{k,\omega}(H + LE)_{k,\omega}. \quad (4)$$

Through Eq. (4), we can examine the component of each term, which coherently varies with (or projects onto) *satellite-estimated* precipitation variations at each wavenumber and frequency.

The reason to bring in satellite precipitation (rather than using ERAI precipitation or multiplying ERAI's own $\langle m^* \rangle$ to obtain its $\langle m \rangle$ variance budget) is that we doubt the accuracy of the reanalysis for these difficult-to-simulate moist tropical phenomena. The ERA-Interim model surely produces its own spectrum of internally generated tropical variability, which may be underconstrained by observations. By projecting ERAI variables onto nearly independently measured precipitation, we isolate the *real-world* signals that (it is hoped) did find their way from reliable observations (such as vapor-sensing satellite data) into the reanalysis.

Geophysical spectra are generally red, meaning that the absolute value of the cross-power spectrum usually decreases with wavenumber and frequency. In addition, it is useful to eliminate the nonintuitive units of Eq. (4). For these reasons, we normalize the contribution of each term in Eq. (4) by the power spectrum of the precipitation itself and by the latent heat of vaporization L,

$$\frac{\overline{P^*_{k,\omega}\left\langle \frac{\partial m}{\partial t} \right\rangle_{k,\omega}}}{L|\overline{P^*_{k,\omega}P_{k,\omega}}|} = \frac{\overline{-P^*_{k,\omega}\langle \mathbf{v}_h \cdot \nabla_h m \rangle_{k,\omega}}}{L|\overline{P^*_{k,\omega}P_{k,\omega}}|} + \frac{\overline{-P^*_{k,\omega}\left\langle \omega \frac{\partial m}{\partial p} \right\rangle_{k,\omega}}}{L|\overline{P^*_{k,\omega}P_{k,\omega}}|} + \frac{\overline{P^*_{k,\omega}\langle Q_R \rangle_{k,\omega}}}{L|\overline{P^*_{k,\omega}P_{k,\omega}}|} + \frac{\overline{P^*_{k,\omega}(H + LE)_{k,\omega}}}{L|\overline{P^*_{k,\omega}P_{k,\omega}}|}, \quad (5)$$

where the overbar indicates the average over time series segments and adjacent wavenumbers and frequencies. Results thus have units of $\mathrm{W\,m^{-2}}$ $(\mathrm{W\,m^{-2}})^{-1}$, or dimensionless, which we will convert to percent for visual convenience in the tables.

d. *Interpretation of the cross-spectrum and its relevance to the GMS*

The gross moist stability (GMS), which was originally introduced by Neelin and Held (1987), is a measure of MSE transport by airflow per unit of latent energy (vapor) lost to precipitation. A variety of versions of GMS have been defined for data reasons or analyst preference. For instance,

entropy rather than MSE may be used as the intensive moist conserved thermodynamic quantity in the numerator, and/or another measure of condensation heating is sometimes used in the denominator (Raymond et al. 2009).

Inoue and Back (2015a) employed a GMS (with symbol Γ) defined as the ratio of column-integrated 3D advection of MSE to column-integrated vertical advection of DSE, because these are estimable from sounding array data:

$$\Gamma = \frac{\langle \mathbf{v}_h \cdot \nabla_h m \rangle + \left\langle \omega \frac{\partial m}{\partial p} \right\rangle}{\left\langle \omega \frac{\partial s}{\partial p} \right\rangle}.$$

Substituting this definition into Eq. (3), the local tendency $\langle \partial m/\partial t \rangle$ is seen to be positive when $\Gamma - \Gamma_c < 0$, and negative when $\Gamma - \Gamma_c > 0$, where Γ_c is the critical GMS (Inoue and Back 2015a) defined as

$$\Gamma_c = \frac{\langle Q_R \rangle + (H + LE)}{\left\langle \omega \frac{\partial s}{\partial p} \right\rangle}.$$

Under the WTG approximation in the tropics, $\langle \partial m/\partial t \rangle \sim \partial \langle m \rangle / \partial t \sim \partial \mathrm{CWV}/\partial t$, as discussed in the introduction, allowing the words moistening and drying to be attached in these situations, respectively. The GMS is highly time dependent (flow dependent), for instance, changing sign through the convective life cycle as the depth of latent heating and upward motion ascends from bottom heavy to top heavy (e.g., Benedict et al. 2014; Hannah and Maloney 2014; Masunaga and L'Ecuyer 2014; Sobel et al. 2014; Inoue and Back 2015a; Sumi and Masunaga 2016; Yokoi and Sobel 2015; Sakaeda and Roundy 2016; and many others). When GMS is extended in this way into the weather realm, from its original use as a "gross" climate diagnostic, this outcome dependence makes the "stability" moniker debatably appropriate [as discussed, e.g., in Sherwood (2000) and Schultz et al. (2000)], but by now it is cemented into the literature.

To clarify the situation, Inoue and Back (2015b) and Inoue and Back (2017) introduced a time-independent (time averaged) "background GMS," and discuss the distinction of two types of GMS (time dependent and time independent). A statistical time average that expresses their background GMS Γ' can be calculated as a least squares linear regression of 3D MSE advection onto vertical advection of DSE s,

$$\Gamma' \equiv \frac{\overline{\langle \mathbf{v}_h \cdot \nabla_h m \rangle' \times \left\langle \omega \frac{\partial s}{\partial p} \right\rangle'}}{\overline{\left\langle \omega \frac{\partial s}{\partial p} \right\rangle'^2}} + \frac{\overline{\left\langle \omega \frac{\partial m}{\partial p} \right\rangle' \times \left\langle \omega \frac{\partial s}{\partial p} \right\rangle'}}{\overline{\left\langle \omega \frac{\partial s}{\partial p} \right\rangle'^2}},$$

where the bar represents a time average and the prime represents departure from the time average. This regression coefficient Γ', a fitted line slope in the "GMS plane" of its independent and dependent variables $\langle \mathbf{v}_h \cdot \nabla_h m \rangle' + \langle \omega \partial m/\partial p \rangle'$ versus $\langle \omega \partial s/\partial p \rangle'$, is the major axis of an ellipse around which the state vector (essentially, CWV) rotates and exponentially amplifies if the radiation feedback and surface flux feedback effects exceed the background GMS (Inoue and Back 2017). Similar regression estimations from data were utilized by Andersen and Kuang (2012) and Adames (2017) to examine which terms of the CMSE budget equation contribute most to the maintenance/dissipation and propagation of the CMSE anomaly (and associated precipitation signal) of the MJO.

The power spectrum of precipitation, which is the denominator in Eq. (5), is another valid measure for the strength of moist convection at a given wavenumber and frequency. Therefore, the column-integrated MSE advection terms in Eq. (5) $[(\overline{-P^*_{k,\omega} \langle \mathbf{v}_h \cdot \nabla_h m \rangle_{k,\omega}}/L|\overline{P^*_{k,\omega} P_{k,\omega}}|) + (\overline{-P^*_{k,\omega} \langle \omega \partial m/\partial p \rangle_{k,\omega}}/L|\overline{P^*_{k,\omega} P_{k,\omega}}|)]$ can be interpreted as another version of a GMS, and since they are constant, they are a background GMS Γ', defined for each discrete wavenumber and frequency. In this sense, our analysis method is comparable to those employed by Inoue and Back (2015b), Andersen and Kuang (2012), Inoue and Back (2017), and Adames (2017). Continuing the analogy, we can say that, on a term-by-term basis, positive real values of terms on the RHS act to amplify disturbances of that frequency and wavenumber, while negative values act to damp them. Likewise for the imaginary component, we may say that a positive (negative) value of the imaginary part of any term on the RHS of Eq. (5) acts to advance (retard) the phase of a disturbance of that particular k, ω (see the appendix for more details). These statements apply to the time-averaged or background GMS Γ' averaged over entire Fourier cycles. A *time-dependent* GMS Γ to measure the local favorability for convection as a function of the phase of a cyclic disturbance would have to be estimated in some residual manner, not attempted here.

We reiterate that precipitation variations are governed or explained in this way only indirectly because they are related to CWV variations, which in turn are related to CMSE because WTG holds to a good approximation. However, because of the scale dependence mentioned above, these two logical dependencies are not equally valid, and the nonlinear CWV–P relationship does not imply a constant proportionality coefficient between anomalies, across the entire spectral domain. In the next section, therefore, the relationship between P and $\langle m \rangle$ variations will be first examined before the tendency terms in Eq. (5) are shown one by one.

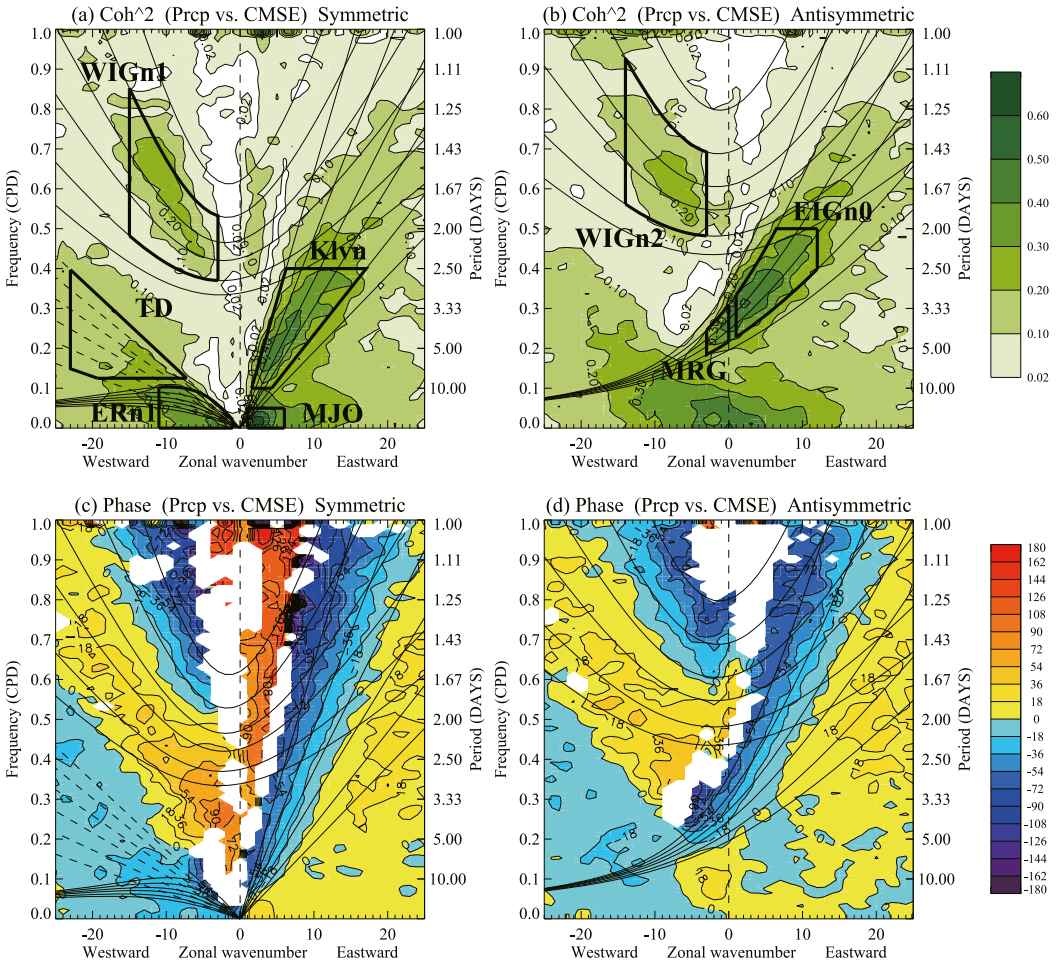

FIG. 1. (a),(b) Space–time coherence squared spectrum and (c),(d) phase spectrum between precipitation and CMSE; (left) symmetric and (right) antisymmetric components. In (a) and (b), the shading and contour interval is 0.1 with the first contour at 0.02, which is significant at the 99% level with 507 DOF. In (c) and (d), the shading and contour interval is 18°, and positive and negative values (shaded with warm and cool colors) mean the column MSE predates and lags rainfall, respectively. Only the area with coherence squared larger than 0.02 is shaded. Dispersion curves are plotted for Klvn, ERn1, WIGn1, WIGn2, EIGn0, EIGn1, and MRG waves with equivalent depths of 8, 12, 20, 30, 50, and 90 m (corresponding to Klvn wave-phase speeds of about 9, 11, 14, 17, 22, and 30 m s^{-1}, respectively). Six dashed lines for the symmetric components indicate constant phase speeds of 3.0, 4.0, 5.0, 6.0, 7.0, and 8.0 m s^{-1}. The region enclosed with thick solid lines represents boxes to evaluate CMSE budgets for each CCEW (see text).

3. Results

a. Precipitation versus CMSE (P versus ⟨m⟩)

Figures 1a and 1b display coherence squared spectra between precipitation and reanalysis CMSE. Although the statistically significant area extends over almost the entire domain, prominent peaks are positioned along with the annotated dispersion curves of the theoretical equatorial waves: $n = 1$ equatorial Rossby (ERn1) wave, Kelvin (Klvn) wave, mixed Rossby gravity (MRG) wave, $n = 0$ eastward inertia–gravity (EIGn0) wave, and $n = 1$, and $n = 2$ westward inertia–gravity (WIGn1 and WIGn2) waves. Peaks associated with MJO and tropical depression (TD)-type disturbances are also evident. Hereafter, we focus on regions around the peaks of the coherence spectrum between precipitation and CMSE, enclosed with thick solid lines in Figs. 1a and 1b. Labels show the contracted name corresponding to each type of disturbance. There is another significant peak of coherence around wavenumber 3 and period of 1.5–2.5 days. However, it does not represent a CCEW disturbance and is left unenclosed (see section 3c).

Figures 1c and 1d show phase spectra between precipitation and CMSE. The area with coherence squared larger than 0.02, which is significant at the 99% level, is

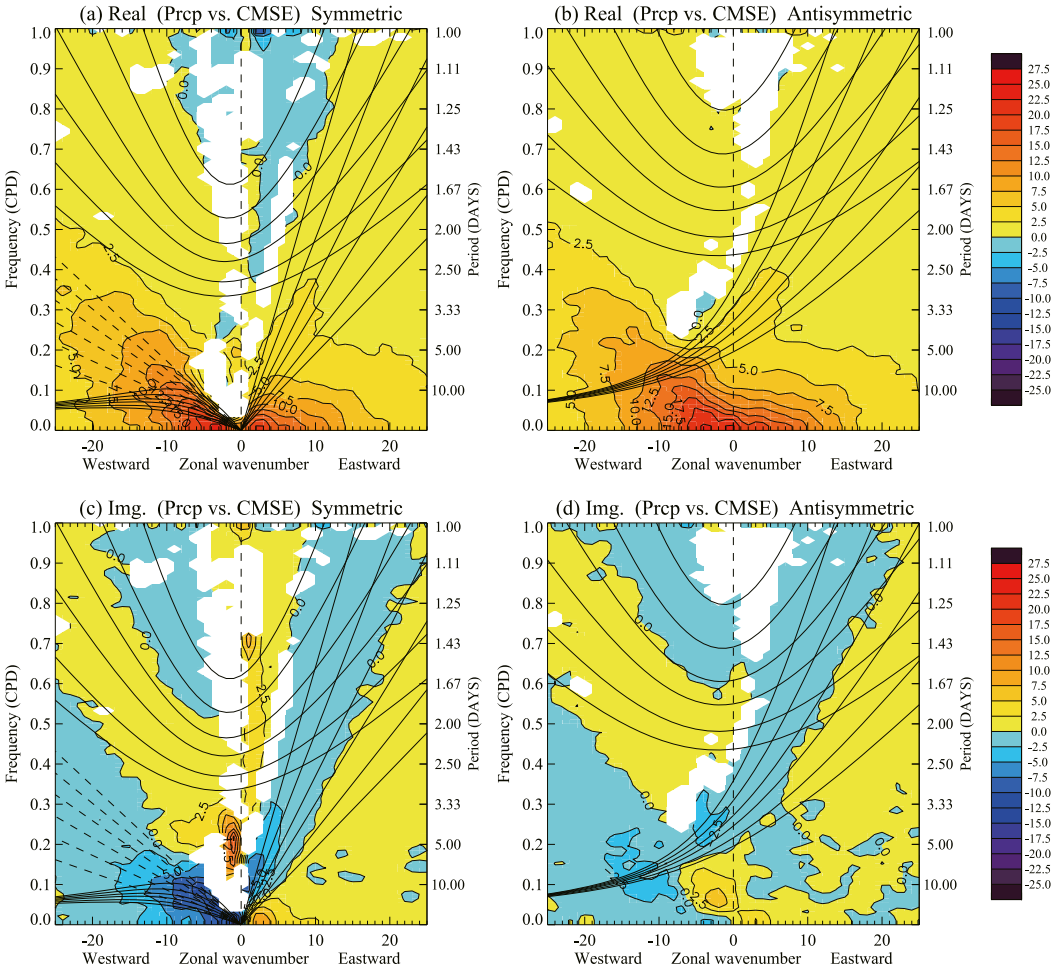

FIG. 2. (a),(b) Real and (c),(d) imaginary components of cross-power spectrum between precipitation and CMSE normalized by the power spectrum of precipitation. The shading and contour interval is 2.5 h, and positive and negative values are shaded with warm and cool colors, respectively. Only the area with coherence squared larger than 0.02 is shaded.

shaded. Positive and negative values of the phase mean that CMSE predates and lags rainfall, respectively (see the appendix for more detail). CMSE lags precipitation around the coherence peak associated with ERn1, Kelvin, MRG, EIGn0 waves, and TD-type disturbances (−26.8° for ERn1, −19.0° for Kelvin, −28.7° for MRG, −7.3° for EIGn0, and −14.1° for TD-type disturbance over the region enclosed with thick solid lines in Figs. 1a,b), while CMSE predates rainfall associated with MJO, EIGn0, and WIG waves (19.3° for MJO, 16.6° for WIGn1, and 4.2° for WIGn2 wave disturbances over the region enclosed with thick solid lines in Figs. 1a,b). The 99% confidence interval for phase difference error is estimated to be about ±14.5° where coherence squared is 0.02 and DOF is 507, so most of the phase differences are statistically distinct from 0. However, we suspect the phase of reanalysis CWV (or CMSE) contains some biases (e.g., Figs. 5 and 6 in Yasunaga and Mapes 2012). Therefore, we still regard it as a valid idea that variations of CMSE and precipitation are basically in phase (at least around the coherent peaks enclosed with thick solid lines in Figs. 1a,b).

An alternate view of the same information is in Fig. 2, which shows real and imaginary components of cross-spectra between precipitation and CMSE. They are normalized by the amplitude of rainfall variation at a given wavenumber and frequency, and, therefore, have the unit of time (hour). The imaginary component of the cross-spectrum (Figs. 2c,d) is smaller than its real component (Figs. 2a,b), reflecting the almost-in-phase relationship we could not reject above. Real components of the cross-spectrum clearly decrease with frequency in Figs. 2a and 2b, meaning that for a given precipitation anomaly, the amplitude of the associated CMSE anomaly is larger for lower-frequency disturbances. This is a familiar result from prior studies (e.g.,

Mapes et al. 2006) and is consistent with the notion that high-frequency waves are orchestrated by wavelike internal density variations, with only a secondary role for moisture anomalies (e.g., Kuang 2008), while moisture storage and transport is essential to, for instance, the MJO (e.g., Adames and Kim 2016).

Having established the nonconstancy (but almost everywhere positive values) of P–CWV correlations across spectral space, so that m budget terms can be interpreted as contributions to precipitation signals, we proceed to examine those terms one by one.

b. *Precipitation versus horizontal advection (P versus $-\langle \mathbf{v}_h \cdot \nabla_h m \rangle$)*

The coherence squared spectrum between precipitation and column-integrated horizontal advection of MSE (Figs. 3a,b) lacks the CCEW peaks seen above. Instead, the most prominent feature is a gently upward–leftward sloping feature in the "TD type" spectral region, predominantly as positive values in the real and imaginary components (Figs. 3c–f). Since TD-type disturbances generally develop in the intertropical convergence zone (ITCZ) of the Northern Hemisphere, the corresponding signal is split between the symmetric and antisymmetric spectra (right and left columns). The slope of the spectral feature agrees with typical easterly wind speeds of a few meters per second, consistent with horizontal advection of localized anomalies (whose Fourier spatial spectrum is, therefore, broad) by mean winds. In addition, the dominance by positive cross power in the imaginary component (Figs. 3e,f) is also indicative of advectively driven propagation (the advance of temporal phase, in Fourier terms) of CMSE anomalies. These are in accord with common experience for such disturbances, including synoptic disturbances over the Pacific Ocean (e.g., Nitta 1970; Wallace 1971; Reed and Recker 1971; Nitta and Takayabu 1985; Liebmann and Hendon 1990; and many others) as well as African "easterly waves" over the Atlantic Ocean (e.g., Carlson 1969; Frank 1969; Burpee 1972, 1974, 1975; Reed et al. 1977; Nitta 1978; and many others). Despite some differences between basins, the results of Fig. 3 are basically similar if the analysis domain is limited over an Indo-Pacific region (45°–225°E) with warm surface temperature (not shown). On the other hand, the evolution of vorticity, which is one of the essential components of the TD-type mode (e.g., Thorncroft and Hoskins 1994; Sobel and Bretherton 1999; Hall et al. 2006), is beyond the scope of the present MSE-based analysis.

Another significant (coherence squared > 0.02) area extends upward–rightward from the MJO region, corresponding to an eastward phase speed of about $4.6\,\mathrm{m\,s^{-1}}$, a speed typical of MJO propagation (e.g., Zhang 2005) and also typical of its westerly wind anomalies. Furthermore, positive imaginary components also indicate that horizontal advection acts to advance the phase of CMSE anomalies associated with MJO, although the real components are negative (meaning that horizontal advection plays a role in damping). Taken together, these results suggest that propagation by horizontal advection of MSE may be one of the essential features that distinguish between dynamical (or equatorial internal density wave) versus nondynamical modes (MJO and TD-type disturbance).

Another interesting feature in Fig. 3a is a peak of coherence near wavenumber 1 (westward) and frequency of 0.2–0.3 cpd, which is not clear in Fig. 1a. Exploring deeper, we found that zonal and meridional winds have barotropic structures at the corresponding wavenumber and frequency and that the horizontal advection of MSE integrated over the troposphere coherently varies with zonal wind in the stratosphere as well as in the troposphere (not shown). Based on previous works (e.g., Hendon and Wheeler 2008; King et al. 2015, 2017), this signal apparently reflects the 5-day Rossby–Haurwitz wave. In fact, Hendon and Wheeler (2008) show that zonal wind associated with the 5-day Rossby–Haurwitz wave lags negative outgoing longwave radiation (OLR) by about 45° and the same-signed phase lag from precipitation (about 70°) is implied at the corresponding wavenumber and frequency in our analysis (not shown, but estimable from Figs. 3c,e). King et al. (2017) found that the 5-day Rossby–Haurwitz wave modulates winds and that precipitation anomalies are strongly correlated with moisture flux convergence in the lower level, but CWV does not show close relationships with those precipitation anomalies, consistent with the absence of this signal in our Fig. 1a.

c. *Precipitation versus vertical advection (P versus $-\langle \omega \partial m/\partial p \rangle$)*

Vertical advection's cross-spectral coherence (Figs. 4a,b) exhibits clear peaks in almost all modes (MJO, ERn1, Kelvin, MRG, EIGn0, WIGn1, and WIGn2 waves), but with relatively weak coherence in low-frequency and TD-type disturbances. The real component of the cross-spectra (Figs. 4c,d) is universally negative in the high-coherence regions, indicating that vertical advection acts to damp these CMSE anomalies. Absolute values are largest in small-wavenumber regions, perhaps a real effect but perhaps indicating that vertical velocity signals associated with satellite-observed precipitation variations are better analyzed (i.e., captured with greater amplitude by the reanalysis system from observational inputs) at larger scales.

Imaginary components (Figs. 4e,f) are positive for Kelvin, MRG, EIGn0, WIGn1, and WIGn2 waves. This means that vertical advection acts to drive horizontal

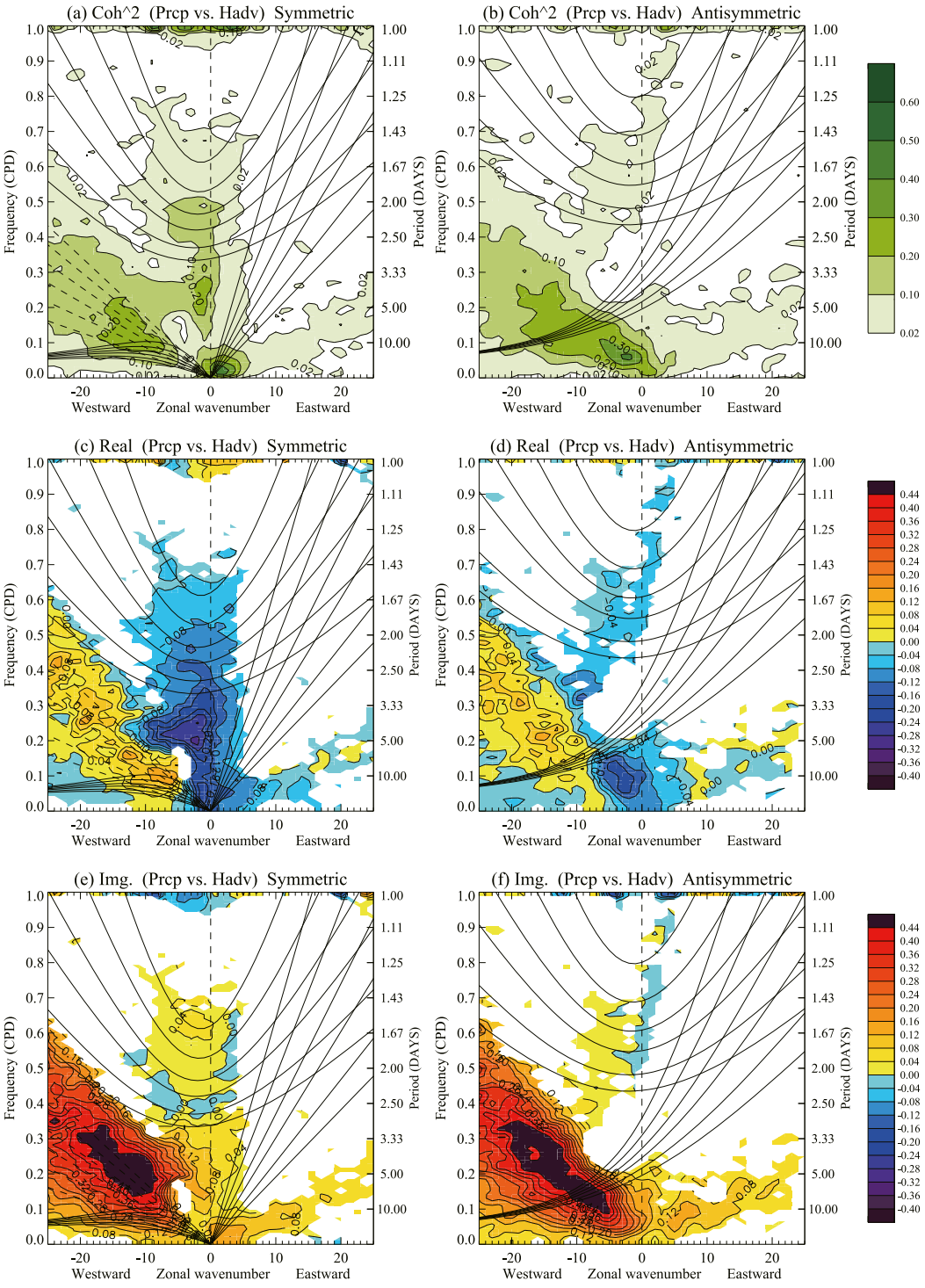

FIG. 3. (a),(b) Space–time coherence squared spectrum and (c),(d) real and (e),(f) imaginary components of the cross-power spectrum between precipitation and column-integrated horizontal advection of MSE normalized by the power spectrum of precipitation ($\overline{-\langle P^*_{k,\omega}\mathbf{v}_h\cdot\nabla_h m\rangle_{k,\omega}}/L|\overline{P^*_{k,\omega}P_{k,\omega}}|$). In (a) and (b), the contour and shading interval is 0.1 with the first contour at 0.02. In (c)–(f), the contour and shading interval is 0.04 W m^{-2} (W m^{-2})$^{-1}$, and positive and negative values are shaded with warm and cool colors, respectively. In (c)–(f), only the area with coherence squared larger than 0.02 is shaded.

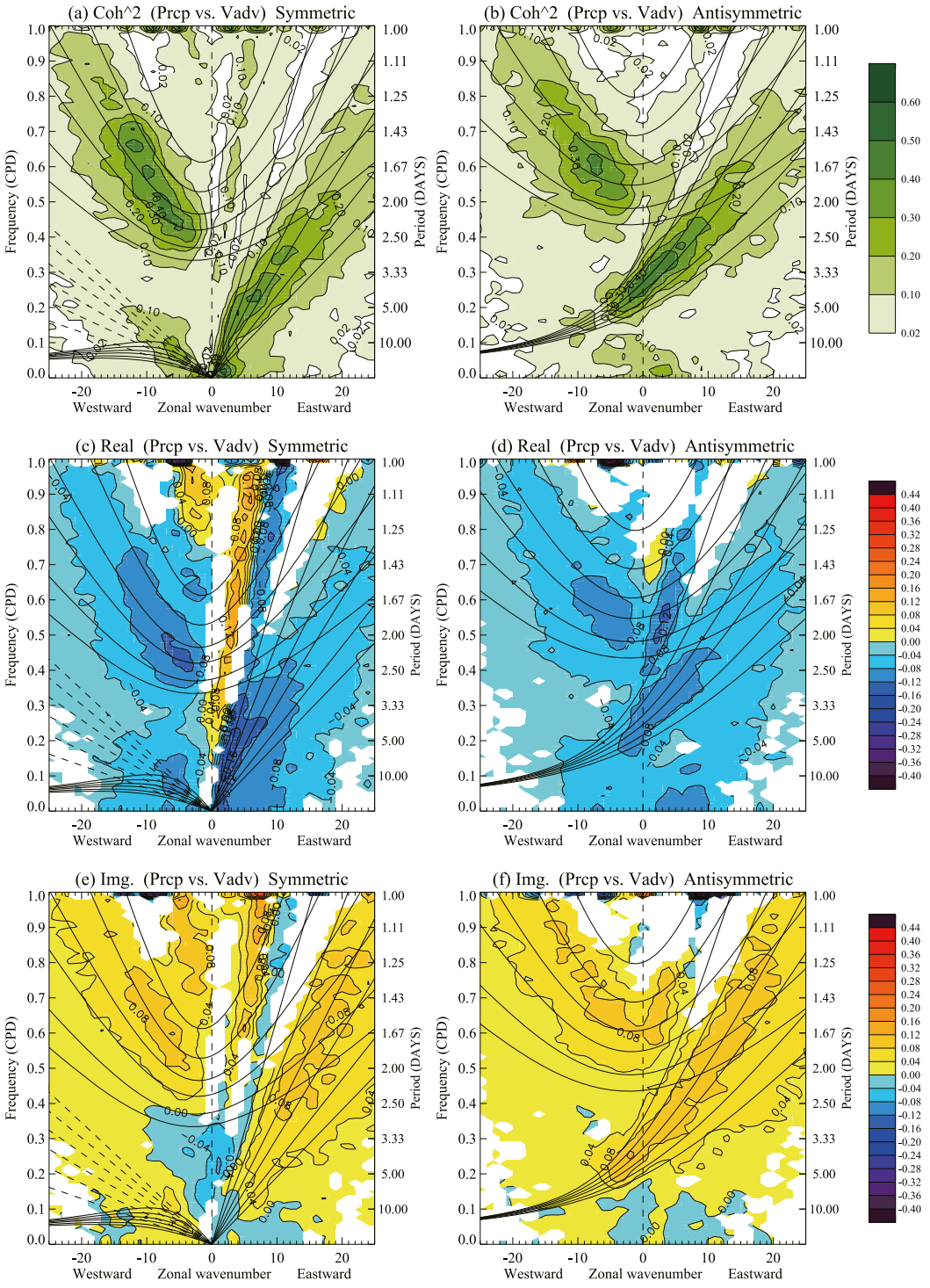

FIG. 4. As in Fig. 3, but for the results from cross-power spectrum between precipitation and column-integrated vertical advection of MSE normalized by the power spectrum of precipitation ($\overline{-P^*_{k,\omega}\langle\omega\partial m/\partial p\rangle_{k,\omega}}\big/L\overline{|P^*_{k,\omega}P_{k,\omega}|}$).

propagation of such wave disturbances (i.e., it acts to advance temporal phase, in Fourier terms). On the other hand, small positive and negative values are found for the ERn1 wave and MJO, respectively, indicating that vertical advection has small (but slightly advancing and retarding) effects on the migration of those oppositely propagating low-frequency variations, that is, driving both types of anomaly westward.

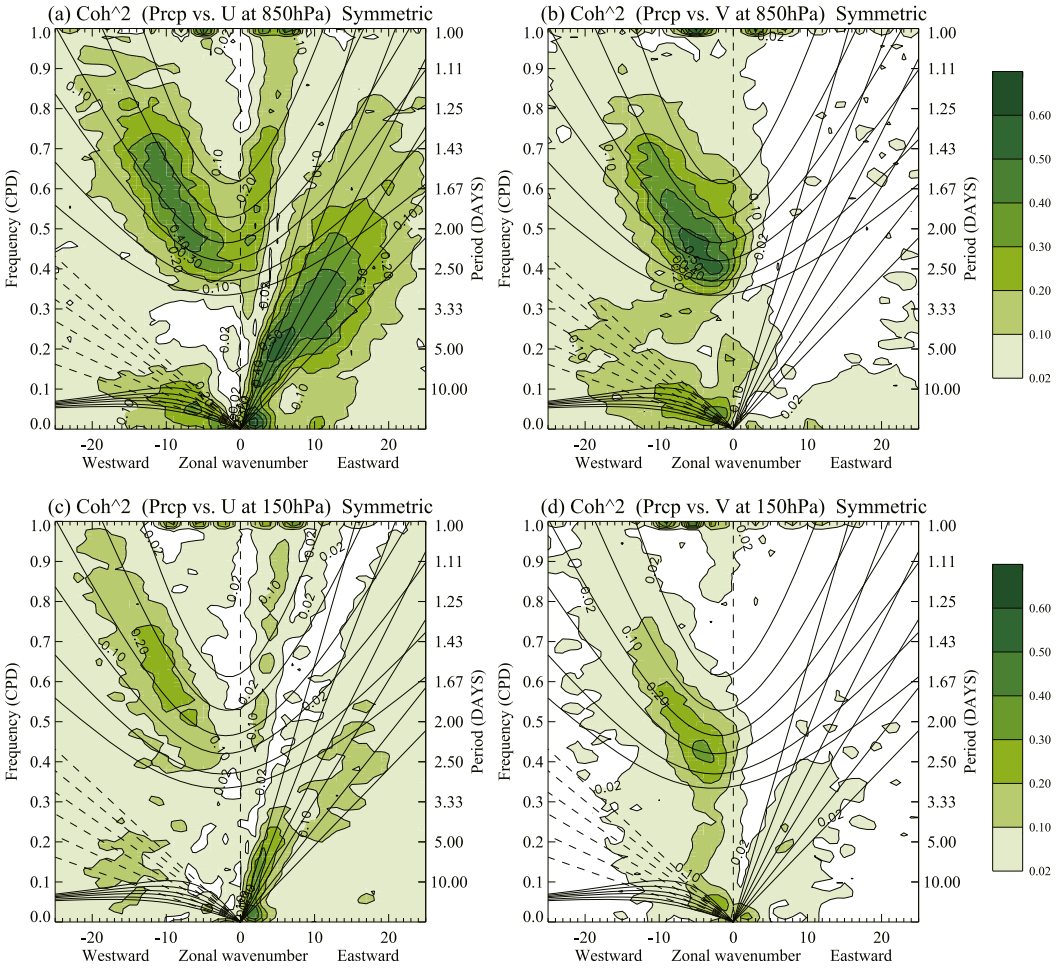

FIG. 5. (a),(c) Space–time coherence squared spectrum between equatorially symmetric precipitation and equatorially symmetric zonal wind at 850 (upper) and 150 hPa (lower) levels. (b),(d) Space–time coherence squared spectrum between equatorially symmetric precipitation and equatorially antisymmetric meridional wind at 850 (upper) and 150 hPa (lower) levels. The contour and shading interval is 0.1 with the first contour at 0.02.

Another notable feature of Fig. 4a is a fast-propagating signal in the eastward direction (around wavenumber 3 and period of 1.5–2.5 days), which is also confirmed in Fig. 1a. The phase spectrum between precipitation and CMSE in this region (Fig. 1c) indicates that CMSE predates precipitation by a little over 90°. Although variations of the MSE vertical advection and precipitation are almost in phase (phase difference is less than 45°, implied by Figs. 4c,e), there is no corresponding peak in the coherence spectrum between precipitation and column-integrated vertical advection of DSE (not shown). This implies that the upward motion associated with the fast-propagating signal is not accompanied with detectable latent heating, although it advects water vapor and thus $\langle m \rangle$ upward. Pursuing this further, Fig. 5 shows significant coherence in this band between precipitation and zonal wind at 150- and 850-hPa levels (Figs. 5a,c) but not meridional wind (Figs. 5b,d). These are hallmarks of a dry Kelvin wave. The propagation speed is estimated as 60–80 m s^{-1}, about double of the typical speed (30–40 m s^{-1}) of relatively fast Kelvin waves in the troposphere (e.g., Bantzer and Wallace 1996; Milliff and Madden 1996; Kikuchi and Takayabu 2003), with an equivalent depth of about 400–600 m, comparable to that of Kelvin wave observed in stratosphere (e.g., Salby et al. 1984; Hitchman and Leovy 1988; Hirota et al. 1991) or in the deep layer spanning troposphere and stratosphere (Matthews and Madden 2000). In fact, significant coherence between precipitation and zonal wind extends to the 50-hPa level but again not for meridional wind (not shown). Some previous works suggest that even fast dynamical waves like atmospheric tides can modulate precipitation (e.g., Yasunaga et al. 2013; Kohyama and Wallace 2016; Sakazaki et al. 2017). However, this apparent modulation of precipitation by vertical motions in a deep dry Kelvin wave in Figs. 1a and 4a might be an artifact of ERAI (e.g., upper-boundary condition),

and further investigation is required for reliable conclusions to be drawn.

d. Precipitation versus radiative heating (P versus $\langle Q_R \rangle$)

Figures 6a and 6b show coherence squared between precipitation and radiative heating. Coherence peaks are seen in almost all modes (MJO, ERn1, Kelvin wave, TD type, MRG, EIGn0, WIGn1, and WIGn2 waves), similar to that between precipitation and CMSE (Figs. 1a,b), consistent with positive anomalies of CMSE, CWV, and the associated clouds acting to reduce OLR.

Positive values of the real component cover almost the entire domain (Figs. 6c,d), indicating that radiation acts to amplify CMSE anomalies associated with any type of disturbance. The value of this positive real component is much greater for low frequencies and large scales. We suspect that precipitation-associated cloudiness may be analyzed too weakly in ERAI data at smaller scales and/or shorter time scales, since cloud is not an assimilated quantity per se but rather depends on assimilated vertical motion as well as moisture. For instance, Fig. 8 of Adames and Kim (2016) indicates from direct satellite observation that OLR per unit precipitation decreases by half (from 0.2 to 0.1) from wavenumber 1 to wavenumber 20 in MJO-related frequencies. Here the comparable slope with wavenumber (albeit of *total* radiative heating) is much steeper (0.16–0.04). This caveat of our data source for $\langle Q_R \rangle$ will be reiterated in the conclusions and should be revisited with more direct observations in a future study.

The imaginary component is slightly negative almost everywhere, but the absolute value is smaller than that of the real part (Figs. 6e,f). This means that the phase difference is close to 0, that is, that variations of the precipitation and radiative heating are almost in phase, with the negative values indicating a physically plausible slight lag of clouds behind precipitation in convective tropical weather.

e. Precipitation versus surface heat fluxes (P versus H + LE)

Figures 7a and 7b show coherence squared between precipitation and surface heat flux. Coherence and signal strengths are both weak, compared with those of radiative heating (Figs. 6a,b), and peaks are only found around MJO, Kelvin, MRG, and EIGn0 waves. It is interesting that the sign of the real and imaginary components of the cross-spectrum are opposite between the MJO and Kelvin waves (Figs. 7c–f), meaning that surface heat flux amplifies and retards MJO anomalies of CMSE, while it damps and advances Kelvin waves. In the antisymmetric components (right column), surface flux slightly damps (blue area) and drives toward the west both the MRG and EIGn0 wave disturbances (advancing the former but retarding the latter, according to the change of sign in Fig. 7f).

Another remarkable feature of Fig. 7 is that there is a maximum of coherence around westward wavenumbers from around −1 to −5 and at the 8–15-day period (Fig. 7a), although a corresponding peak is not found in coherence between precipitation and CMSE (Fig. 1a). The real component of the cross-spectrum is large and positive here, while the imaginary component is weaker and negative (Figs. 7c,e), indicative of variations of surface heat flux that are in phase with (or slightly lagging behind) precipitation variations. This peak is also robust even if the analysis domain is limited over the oceanic region (45°–225°E) with warm surface temperature (not shown). Yasunaga et al. (2010) reports that diurnal variations of the sea surface temperature were enhanced in light-wind and clear conditions over the tropical Indian Ocean and suggests that the observed modulation was associated with westerly anomalies with a deep nearly barotropic structure through the troposphere. The coherence peak in Fig. 7a might reflect modulation of surface winds and precipitation by such barotropic disturbances. Further investigations are required to draw firmer conclusions about this intriguing signal.

4. Decomposition of the advection terms

Theoretical wave models, a pillar of understanding, require base state assumptions as part of their framing. To better inform such efforts, we further explored the effects of partitioning MSE advection into time and space mean, time mean, and all remaining variations, as follows:

$$m = \overline{\overline{m}}(p) + \overline{m}(\mathbf{x}, p) + m'(\mathbf{x}, p, t),$$

where $\overline{\overline{m}}$, $\overline{m}$, and m' are the time and 15°S–15°N mean profile of MSE, the time mean of $m - \overline{\overline{m}}$ (“stationary eddy” structure), and the remainder, respectively. Using this definition, the cross-spectrum of horizontal and vertical advection (computed at each latitude–longitude location $\mathbf{x}$ and then averaged over the 15°S–15°N belt) can be expanded as

$$\frac{-P^*_{k,\omega}\langle \mathbf{v}_h \cdot \nabla_h m \rangle_{k,\omega}}{L|P^*_{k,\omega} P_{k,\omega}|} = \frac{-P^*_{k,\omega}\langle \mathbf{v}_h \cdot \nabla_h \overline{m} \rangle_{k,\omega}}{L|P^*_{k,\omega} P_{k,\omega}|} + \frac{-P^*_{k,\omega}\langle \mathbf{v}_h \cdot \nabla_h m' \rangle_{k,\omega}}{L|P^*_{k,\omega} P_{k,\omega}|},$$

and

$$\frac{-P^*_{k,\omega}\left\langle \omega \frac{\partial m}{\partial p} \right\rangle_{k,\omega}}{L|P^*_{k,\omega} P_{k,\omega}|} = \frac{-P^*_{k,\omega}\left\langle \omega \frac{\partial \overline{m}}{\partial p} \right\rangle_{k,\omega}}{L|P^*_{k,\omega} P_{k,\omega}|} + \frac{-P^*_{k,\omega}\left\langle \omega \frac{\partial \overline{m}}{\partial p} \right\rangle_{k,\omega}}{L|P^*_{k,\omega} P_{k,\omega}|} + \frac{-P^*_{k,\omega}\left\langle \omega \frac{\partial m'}{\partial p} \right\rangle_{k,\omega}}{L|P^*_{k,\omega} P_{k,\omega}|}.$$

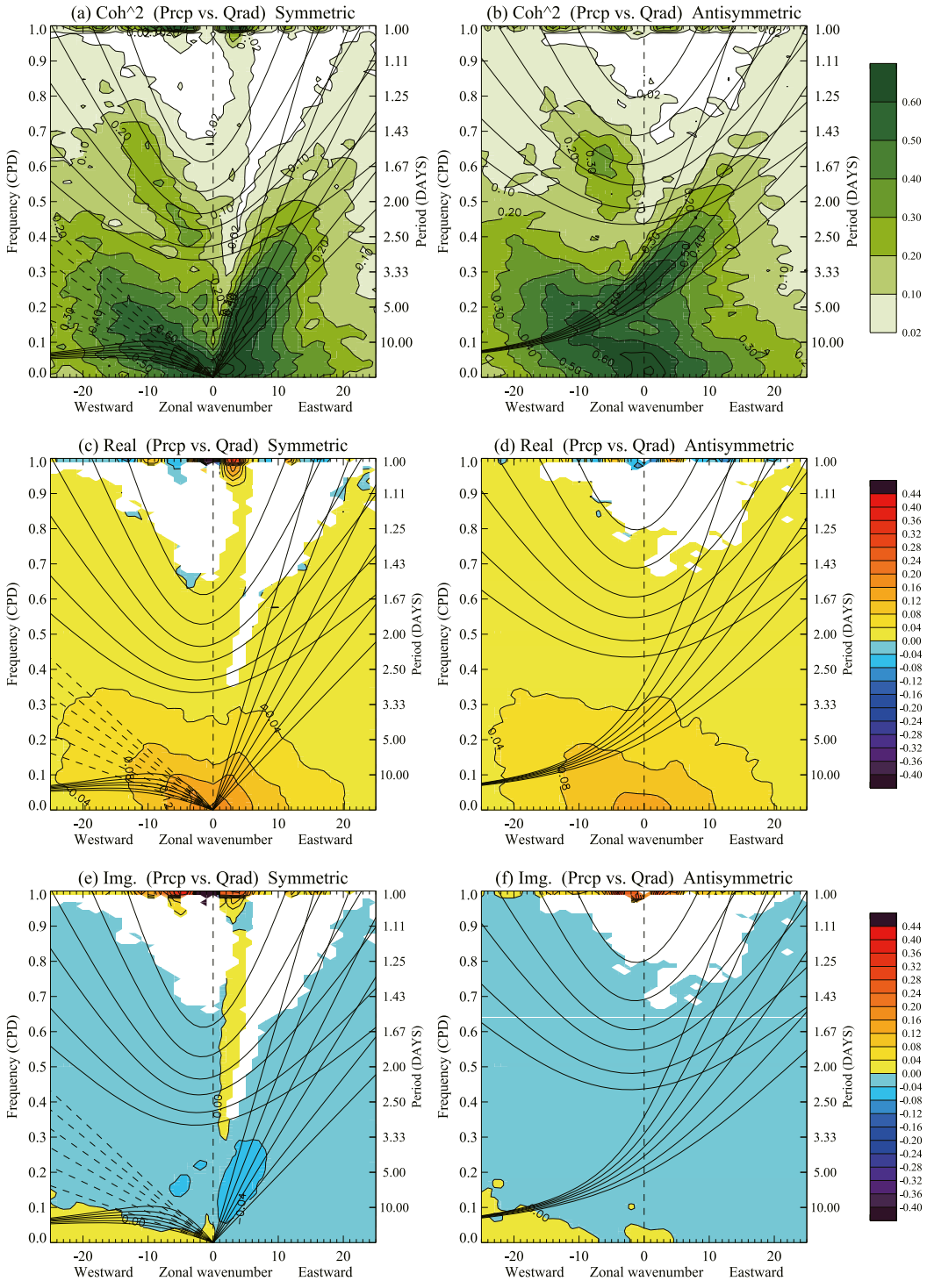

FIG. 6. As in Fig. 3, but for the results from cross-power spectrum between precipitation and column-integrated radiative heating ($\overline{P^*_{k,\omega}\langle Q_R\rangle_{k,\omega}}/L|\overline{P^*_{k,\omega}P_{k,\omega}}|$).

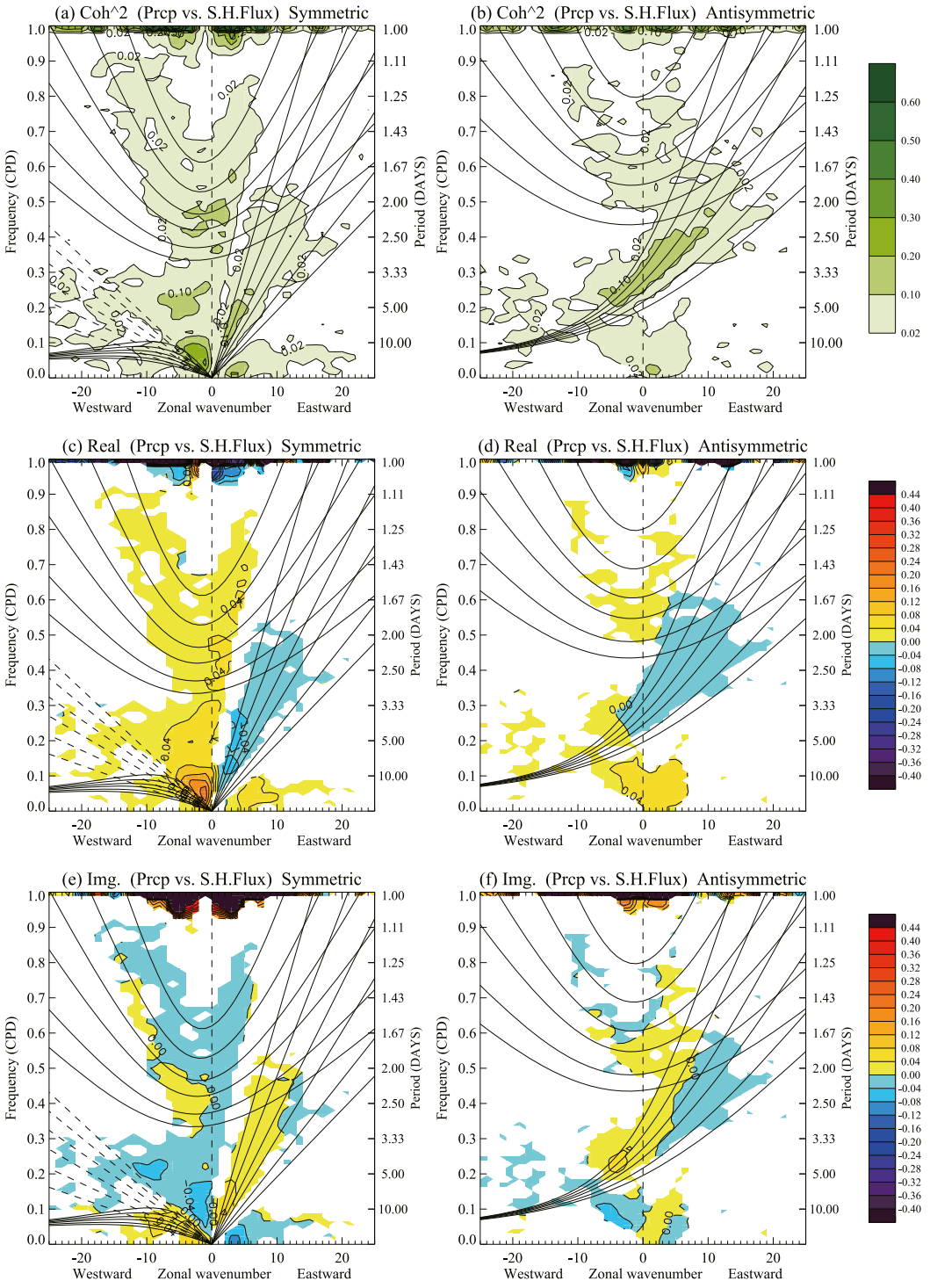

FIG. 7. As in Fig. 3, but for the results from cross-power spectrum between precipitation and surface heat flux $[\overline{P^*_{k,\omega}(H+LE)_{k,\omega}}/L|\overline{P^*_{k,\omega}P_{k,\omega}}|]$.

If a total advection effect from Fig. 3 or Fig. 4 is adequately explained by advection of one of the mean m fields, a theory based on that assumption could be used to clarify the implied mechanisms in an idealized way. On the other hand, if a signal appears in two terms on the right, but in a cancelling manner so that it is not present in total advection, then the decomposition is an unsuitable basis for theory. Of course, further decompositions could also be

made of the velocity term in the advection product, and/or by separating horizontal and meridional advection terms, but such a diagnosis would not serve theory in this way and we have not done it. As a result, interpretation of these decomposed terms is sometimes not specific. For instance, we cannot distinguish simple advection of wave-scale anomalies by a mean flow, wave-scale nonlinearity (self-advection), and possible rectified subwave-scale eddy effects that might be part of putatively "hierarchical" multiscale wave structures. Although such distinctions are beyond the current scope, a few possibilities are noted when the terms are presented below.

a. *Precipitation versus horizontal advection of decomposed MSEs*

Horizontal advection of time-mean MSE $\overline{m}$ (Fig. 8) shows coherence peaks around ERn1 and WIG waves (Figs. 8a,b), although corresponding signals are missing (or much weaker) for horizontal advection of total MSE (Figs. 3a,b). Conversely, the peaks around TD-type disturbance and MJO, which are clear in Figs. 3a and 3b, are weaker or missing in Figs. 8a and 8b.

The real component of the cross-spectrum is positive for MJO and ERn1 wave, indicating that advection of time-mean MSE gradients plays a role in amplifying CMSE anomalies associated with MJO and ERn1 wave disturbance (Figs. 8c,d). Meanwhile, the signs of the imaginary component are opposite (positive for MJO and negative for ERn1 wave) in Figs. 8e and 8f, meaning that advection of stationary components in moisture helps both of the MJO and ERn1 wave disturbances migrate eastward. These results are consistent with those obtained by previous theoretical works. Sobel et al. (2001) discuss the importance of the background moisture field to the propagation of low-frequency mode. Adames and Kim (2016) found that horizontal advection of mean moisture by the anomalous winds associated with ERn1, on the eastern side of the precipitation peak within that disturbance, is one of the keys for the eastward migration of that planetary-scale disturbance. Here total advection is found to be of opposite sign to that advection of the long time-mean gradient (noting the opposite signs around ERn1 wave spectral region in Figs. 3e, 8e).

Blue areas just left of center in both Figs. 3c and 8c indicate that the total horizontal advective damping of WIG waves (Fig. 3c) is partly due to advection of stationary (climatological) MSE. Both zonal and meridional winds in the lower troposphere have significant coherence in the corresponding region (e.g., Figs. 5a,b). Since meridional gradients of mean moisture field are generally larger than its zonal gradient, meridional advection might be thought to explain this advective damping of WIG wave disturbances. However, Sumi and Masunaga (2016) claimed that zonal advection of anomalous moisture has larger effects than meridional advection in the WIGn1 wave disturbance. Meanwhile, their filtering box is rather large (cf. our Fig. 1a to Fig. 1 of Sumi and Masunaga 2016), so reconciling this point is not possible without further decompositions of advection, a useful topic for a future study.

Horizontal advection of the remainder pattern $m'(\mathbf{x}, t, p)$ in Fig. 9 qualitatively explains most of the features of total advection in Fig. 3, indicating that time-mean spatial structure is a secondary effect (as evidenced by relatively small magnitudes in Fig. 8), except at the lowest frequencies where the real parts of Figs. 9c and 9d are opposite in sign to Figs. 8c and 8d. The damping by this remainder advection (negative values at the bottom of Figs. 9c,d) is intriguing even though it is weak in total advection (Figs. 3c,d) because of a compensating positive effect of background gradients $\overline{m}(\mathbf{x}, p)$ (positive values at the bottom of Figs. 8c,d). Might it reflect a rectified effect of subwave-scale eddies? Others have found that synoptic-scale eddy activity is enhanced in westerly phases of MJO (e.g., Takayabu and Murakami 1991; Maloney and Hartmann 2001; Maloney and Dickinson 2003), causing drying around the precipitation peak. Sobel and Maloney (2013) and Adames and Kim (2016) incorporated such an effect of anomalous moistening and drying by high-frequency eddies in their linear MJO models and successfully obtained planetary-scale unstable solutions. Further decomposition of advection could clarify whether Fig. 9 is indicative of such a rectified eddy effect as opposed to some wave-scale advective effect.

b. *Precipitation versus vertical advection of decomposed MSEs*

Three terms are involved in decomposed vertical advection. Figure 10 shows cross-spectra when analyzed vertical motion is treated as if it "advects" the whole-tropics time-mean MSE $\overline{\overline{m}}(p)$. General features in Fig. 10 are same as those seen in total advection (Fig. 4), but stronger, especially in the real component (negative, indicating wave amplitude damping). The values of coherence are about 1.5 times larger and all peaks are present. Only vertical velocity ω fluctuates in this term, and ω is coherent with precipitation for all wave types, like radiation (Figs. 6a,b).

Vertical advection of spatially patterned but time-mean MSE $\overline{m}(\mathbf{x}, p)$ also exhibits a coherence pattern (Figs. 11a,b) similar to Figs. 10a and 10b, since again only ω fluctuations enter the temporal FFT. In contrast, the term expressing advection of the remainder $m'(\mathbf{x}, p, t)$ (Figs. 12a,b) exhibits less coherence at high frequencies. We speculate that this is because the product of two

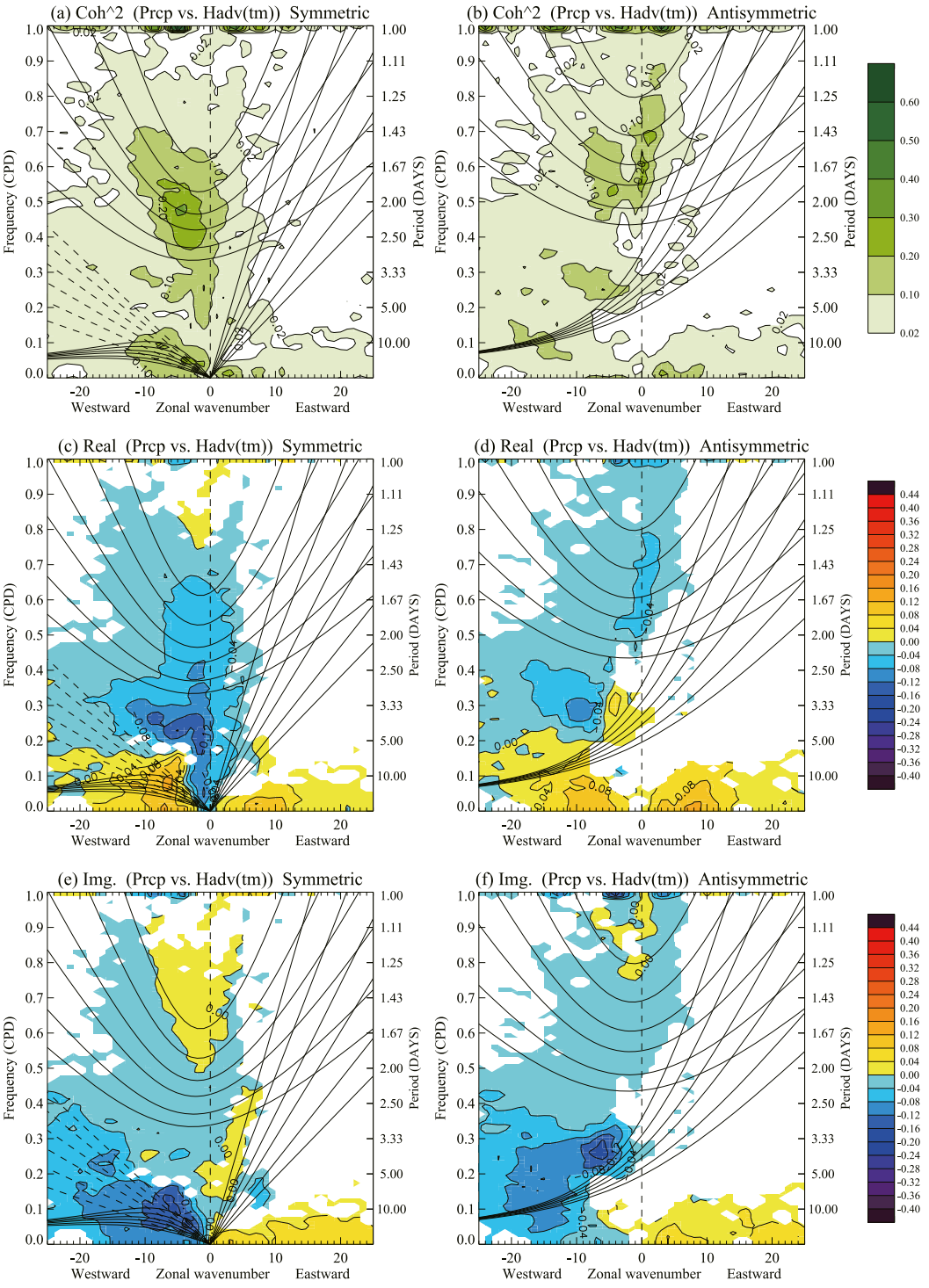

FIG. 8. As in Fig. 3, but for the results from cross-power spectrum between precipitation and column-integrated horizontal advection of time-mean MSE $\overline{m}(\mathbf{x}, p)$.

temporally fluctuating terms has more noise (as well as perhaps less signal) at high frequencies.

Figures 11 and 12 are both corrections to the fictitious and erroneous vertical advection process in Fig. 10, relative to true advection (Fig. 4). In the real component, both are *positive* over the entire domain (Figs. 11c,d, 12c,d). Averaging over the whole tropics erroneously decreases and increases the value of moisture compared to its true

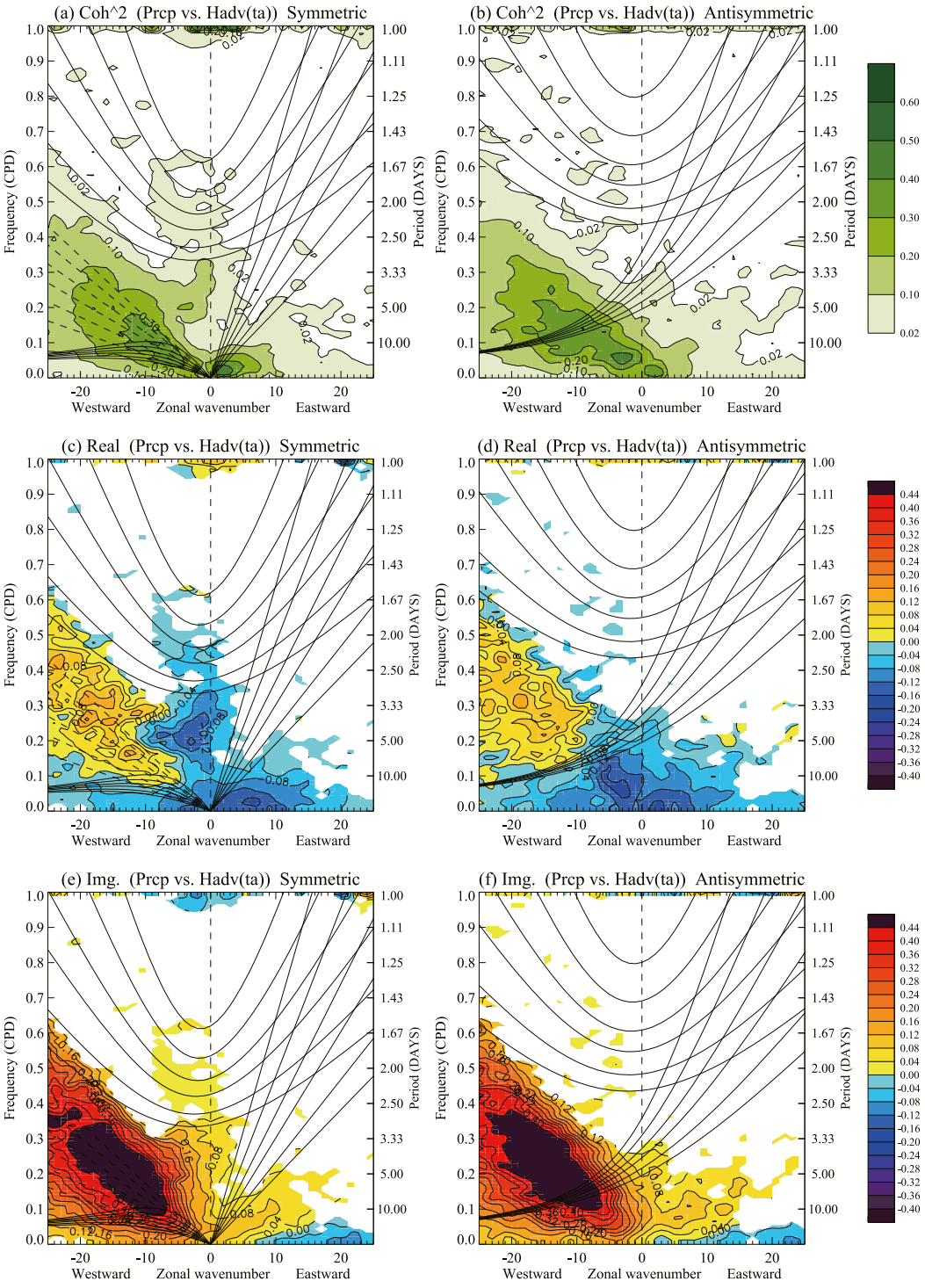

FIG. 9. As in Fig. 3, but for the results from cross-power spectrum between precipitation and column-integrated horizontal advection of the anomaly from time-mean MSE $m'(\mathbf{x}, p, t)$.

values in ascending and descending regions, respectively. This leads to underestimated (overestimated) moisture convergence in the moist ascending (dry descending) regions, which makes the damping effect in Figs. 10c and 10d drastically too strong. Figures 11c, 11d, 12c, and 12d are successive partial corrections to that drastic error. This correction could also be understood from consideration of vertical motions in the moist environments around

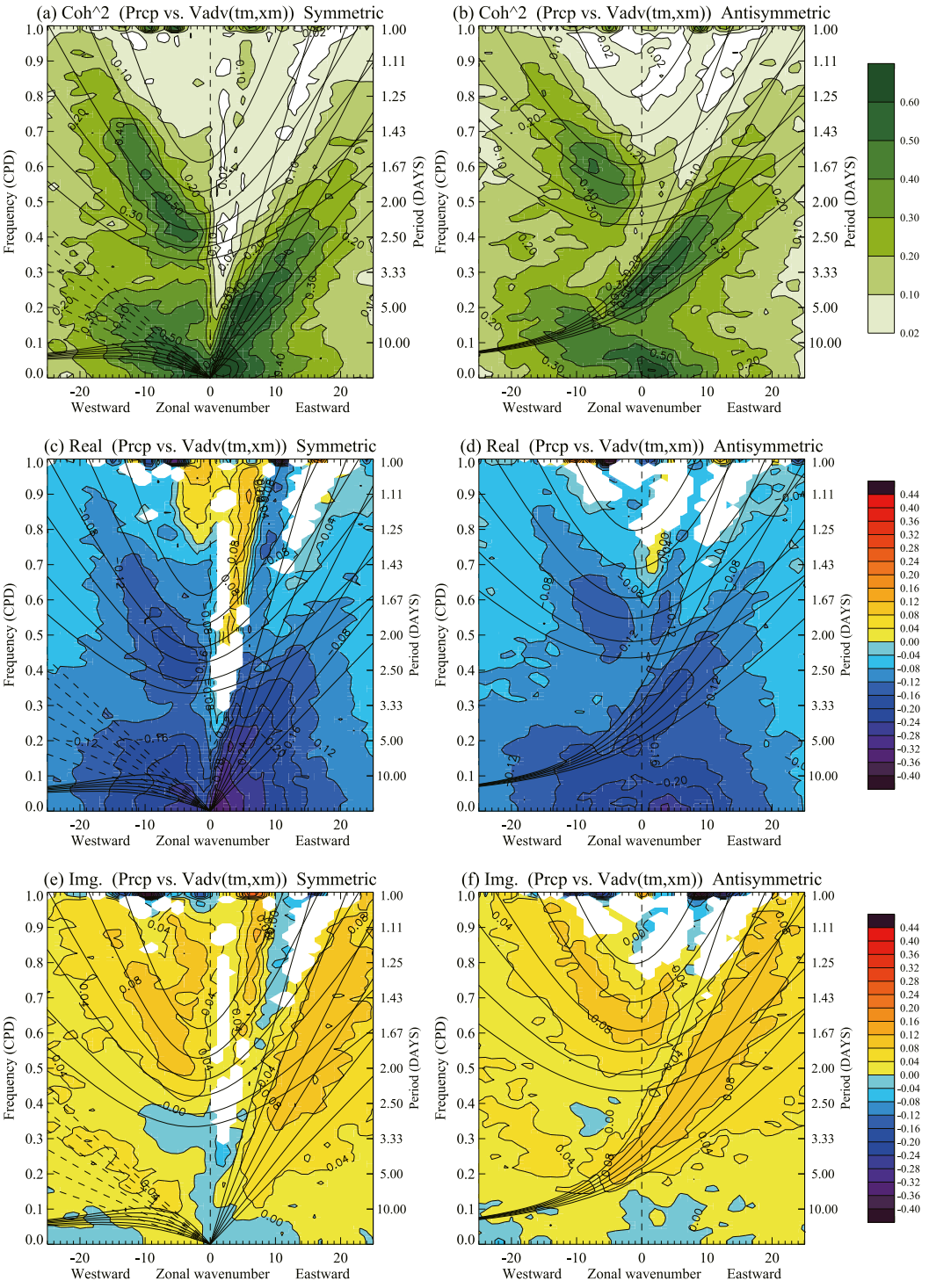

FIG. 10. As in Fig. 3, but for the results from cross-power spectrum between precipitation and column-integrated vertical advection of time–zonal-mean MSE $\overline{\overline{m}}(p)$.

precipitation versus in an average (drier) environment: ascending (descending) regions are in more humid (drier) environments than average in time as well as in space. The relatively larger values in Fig. 12 than Fig. 11 indicate that the humidity of an ascending (or descending) region is due more to temporal than to merely spatial variations. This correction is greatest for low frequencies, which have the largest humidity anomalies per unit precipitation, as

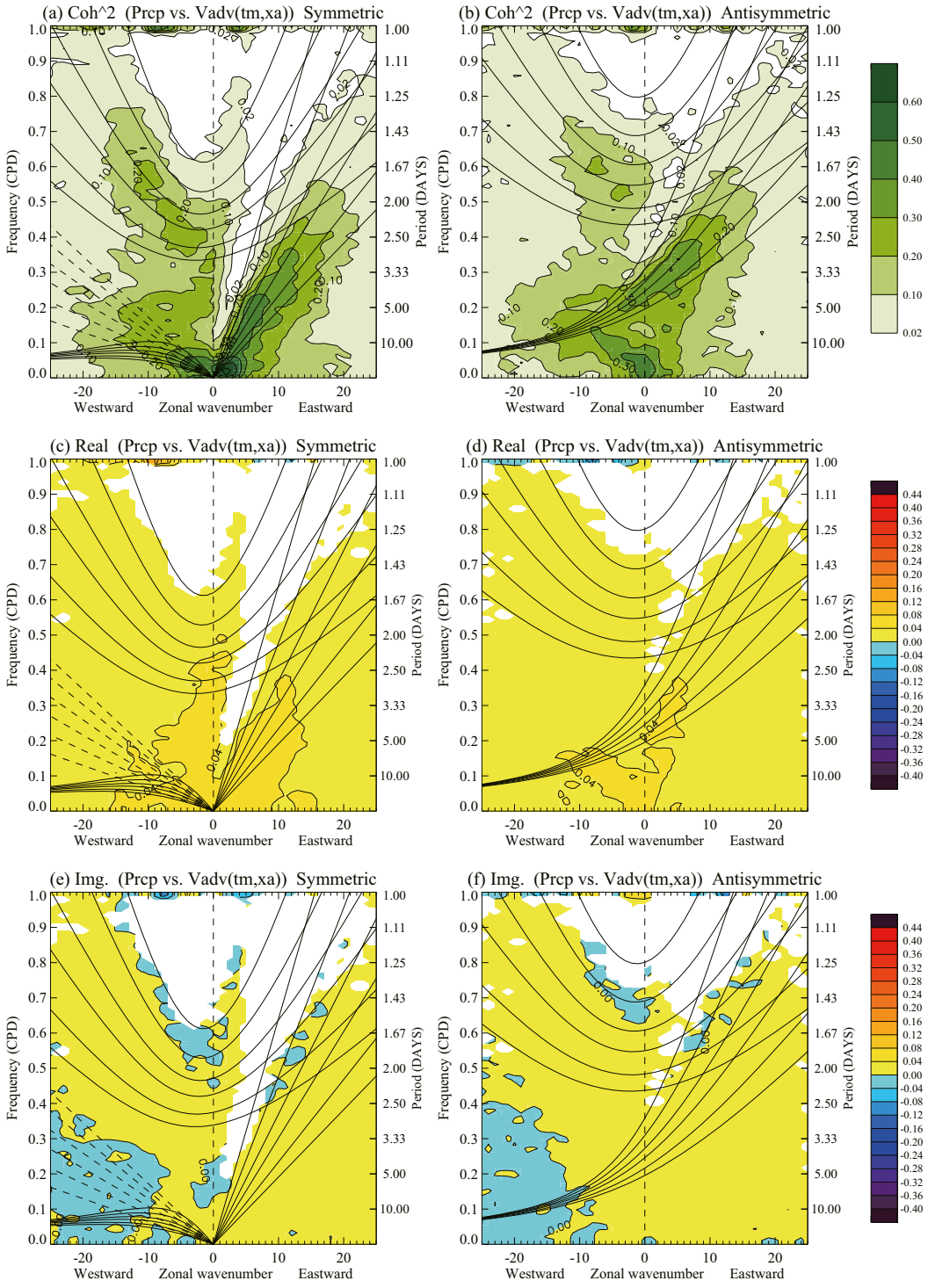

FIG. 11. As in Fig. 3, but for the results from cross-power spectrum between precipitation and column-integrated vertical advection of zonal perturbations of the time-mean MSE $\overline{m}(\mathbf{x}, p)$.

discussed around Figs. 2a and 2b. Therefore, positive correlations of the moisture and vertical motion might be essential to such low frequencies and large-scale disturbances. However, the aforementioned (further) decomposition of vertical wind is needed to confirm speculation about interpretation of this positive nonlinear feedback, although the contribution of climatological wind is generally small for vertical advection.

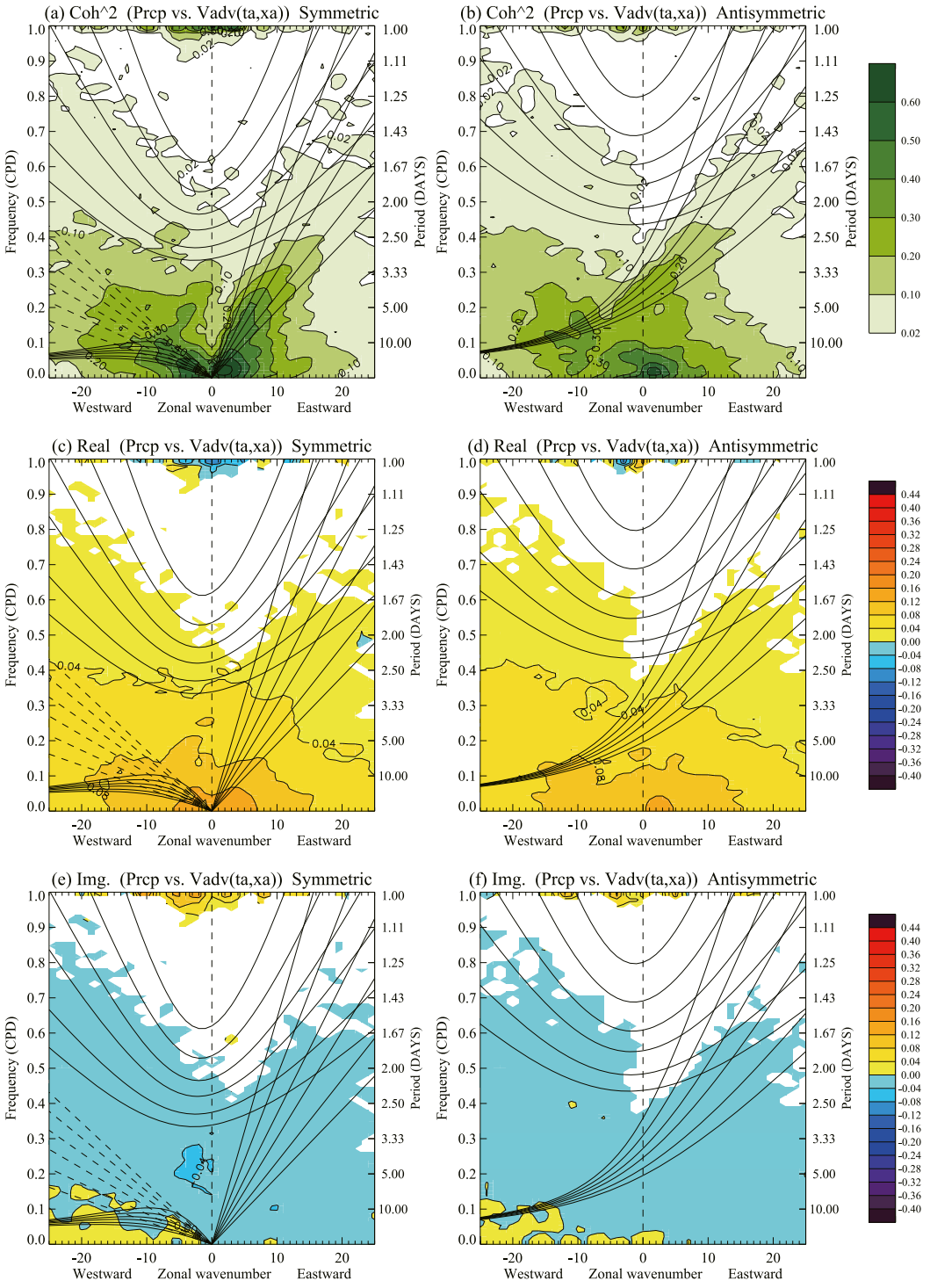

FIG. 12. As in Fig. 3, but for the results from cross-power spectrum between precipitation and column-integrated vertical advection of the anomaly from the time-mean MSE $m'(\mathbf{x}, p, t)$.

The importance of moisture accession by cumulus congestus clouds and the associated bottom-heavy ascent by their latent heating has been emphasized for the moistening in the MJO developing phase (e.g., Johnson et al. 1999; Kikuchi and Takayabu 2003; Mapes and Bacmeister 2012; Bellenger et al. 2015; and many others). If the wave-phase dependence of top heaviness of ω is misanalyzed in ERAI, this profile-dependent effect might

also be misestimated. On the other hand, it should be noted that the assumption of no correlations between cloud-scale horizontal wind and moisture and temperature perturbations in Eq. (3) excludes the effect of the vertical MSE advection by the (model unresolvable) cloud-scale motion.

Imaginary signals in Figs. 11 and 12 are too small to discuss, but are displayed for completeness.

5. Synthesis

To complete our synthesis, Fig. 13 shows the residual term's cross-spectra in identical form to previous figures. Coherence shows especially significant signals around the Kelvin and EIGn0/MRG wave regions. The residual real component is generally negative except for the relatively high-coherence regions (Kelvin and EIGn0/MRG wave), while the residual imaginary component is systematically positive.

This concludes our survey of terms in the CMSE budget of tropical disturbances in spectral space. To summarize them, real and imaginary components of Eq. (5) are summed over the mask area corresponding to each type of the disturbance (annotated in Figs. 1a,b). For clarity, we shall multiply by 100 in the tables below to express these precipitation-associated CMSE tendencies as percentages of total latent heat release at the corresponding wavenumber and frequency.

Table 1 contains the real component, indicative of amplification or damping. All these types of *P*-correlated CMSE disturbance are amplified by radiation and damped by vertical advection, although the relative contributions are different. Decomposition indicates that the vertical advective damping is much less than it would be if the MSE profile (moisture profile) were the tropical mean, or even the time mean, at each location: In other words, the temporal correlation between moisture and ascent is a first-order positive feedback for all kinds of Fourier disturbances of the observed amplitude. Such quadratic or correlation terms are ignored in linear models, which makes those further from observationally comparable relevance. It should be noted that the advection of wave-scale MSE anomaly by the background or climatological wind is included in our "eddy component," although the contribution is small for vertical advection.

The imaginary or quadrature component (Table 2) summarizes the effect of each term on *propagation* (temporal phase advancement) of precipitation-associated CMSE anomalies. Here the residual is larger (on the order of 5% rather than on the order of 1% of the real component, except for the ERn1 and TD mode). These large residuals imply that the reanalysis procedure and/or the underlying model physics may be poorer at propagating the analyzed anomalies than at closing its basic precipitation-associated MSE budget. It should also be noted that residuals are dominantly *positive*. A positive value of the residual means that phase-advancing or forward-propagation effects by some or all physical terms are underestimated. One candidate for this systematic error could be a poor analysis of vertical velocity. Such a poor analysis could involve the magnitude (too weak or insufficiently precipitation correlated), since the effect of vertical advection is also mostly positive. But it could also involve the profile, for instance, if the analyzed ascent in cloudy disturbances fails to be sufficiently bottom heavy in the front of disturbances and top heavy in the rear, as seen in observational studies on a range of time scales (Mapes et al. 2006).

The residual real component is small in most named wave regions, compared with the residual imaginary component, as seen in Tables 1 and 2. However, it is likely that this residual could also include compensating errors, since it is the sum of all model errors. For instance, we have insinuated that the magnitudes of both vertical velocity and cloudy radiation may be underanalyzed for smaller-scale *P*-correlated weather features (values too small on the right and left edges of Figs. 4 and 6). Because the sign of these effects systematically cancels, and they are physically linked in the model (which could make their scale-dependent analysis errors similar in magnitude), the small residual in Table 1 may not indicate a lack of problems in the real component. Only additional studies with other reanalysis, radiative heating, and/or precipitation datasets can resolve this doubt, and this caveat should be borne in mind for further discussions below.

a. MJO and ERn1 wave disturbances

The MJO and ERn1 wave filter regions are significantly amplified by radiation (14.3% and 12.1%, respectively) and more weakly by surface heat flux (2.5% and 2.8%, respectively), while they are damped by vertical advection (11.4% and 7.5%, respectively). Although MJO and ERn1 wave disturbances share similar features of the real component, they differ in sign regarding the effect of horizontal advection (−10.1% and 2.9%, respectively). Decomposition indicates that horizontal advection of time-mean MSE tends to amplify MJO and ERn1 wave disturbances, although they are damped by the eddy component. The eddy-damping effects are especially remarkable for MJO, since the contribution is largest among all types of disturbance and is comparable to that of total vertical advection.

The extended cover of clouds in moist regions reduces the longwave emission from Earth to space, causing

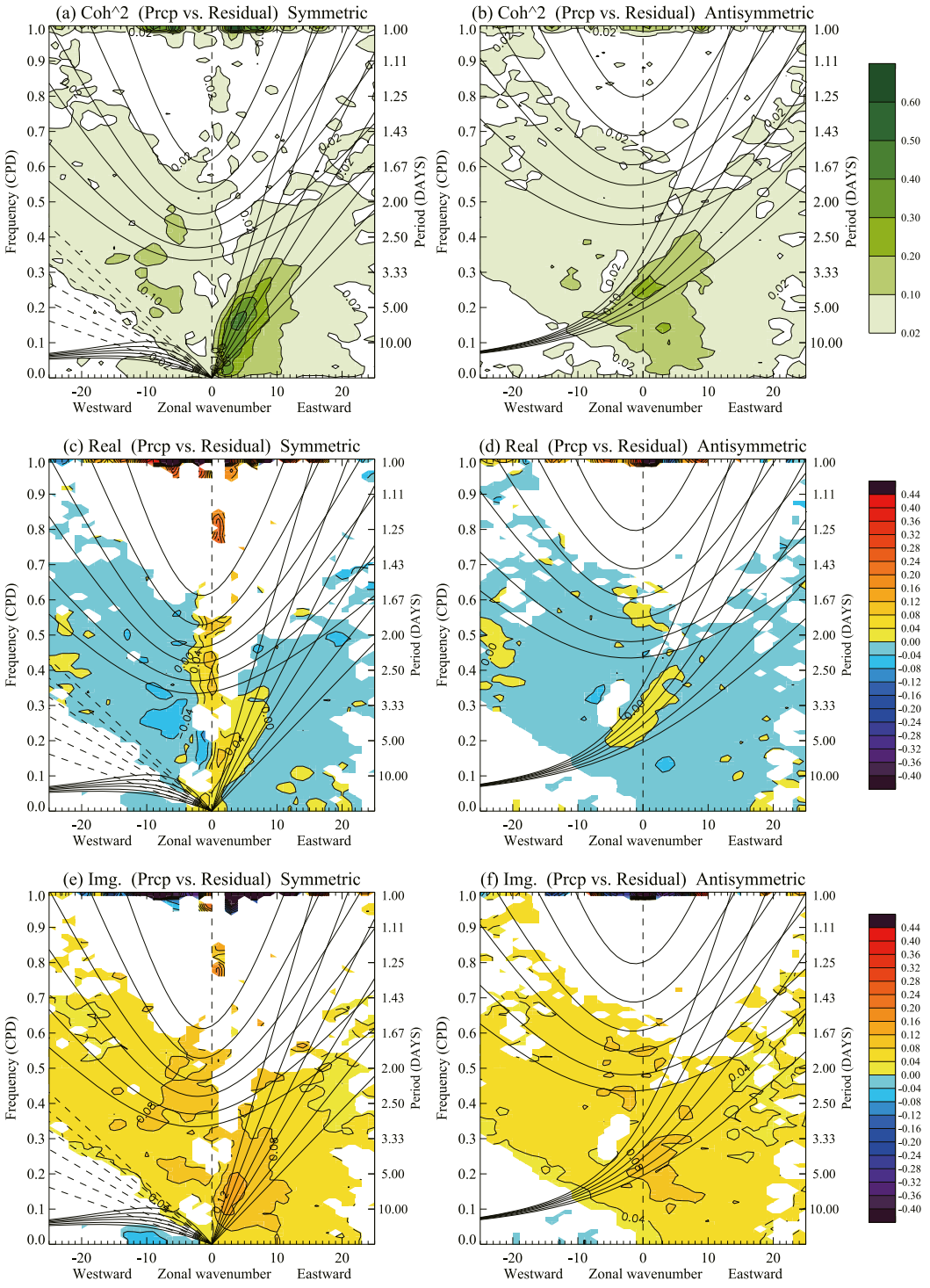

FIG. 13. As in Fig. 3, but for the results from cross-power spectrum between precipitation and residual in the column-integrated MSE budget equation.

anomalous heating. Numerous theoretical or observational investigations invoke the cloud radiation feedback to growth of intraseasonal time-scale disturbances like MJO (e.g., Raymond 2001; Bretherton and Sobel 2002; Tian and Ramanathan 2003; Lin and Mapes 2004; Bony and Emanuel 2005; Zurovac-Jevtić et al. 2006; Ma and Kuang 2011; Sobel et al. 2014; Sobel and Gildor 2003; Kim et al. 2015; Adames and Kim 2016). Our

TABLE 1. The real component of the cross-spectrum between precipitation and each term of Eq. (5) summed over the area corresponding to the disturbances associated with ERn1, Klvn, MRG, EIGn0, and WIGn1 and WIGn2 waves as well as the MJO and TD-type mode. The area associated with each disturbance is enclosed with thick solid lines in Figs. 1a and 1b. In the table, bold (italic) text indicates that the sign of the value is statistically significant (insignificant) at the 99% confidence level (DOF 126). All the values are increased by a factor of 100, and the unit is $\mathrm{W\,m^{-2}\,(W\,m^{-2})^{-1}} \times 100$.

	WIGn1	TD	ERn1	MJO	Klvn	WIGn2	MRG	EIGn0
$\left\langle \frac{\partial m}{\partial t} \right\rangle$	**−13.1**	**7.7**	**9.1**	**−6.0**	**−11.0**	**−9.2**	**−4.2**	**−9.2**
$-\langle \mathbf{v}_h \cdot \nabla_h m \rangle$	**−4.9**	**5.5**	**2.9**	**−10.1**	**−2.0**	**−2.6**	*−0.6*	*−1.0*
$-\langle \mathbf{v}_h \cdot \nabla_h \overline{m}(x) \rangle$	**−2.8**	*−1.1*	**8.0**	**4.2**	**−1.2**	**−1.7**	**2.5**	*−0.5*
$-\langle \mathbf{v}_h \cdot \nabla_h m'(x,t) \rangle$	*−2.1*	**6.6**	**−5.2**	**−14.3**	*−0.9*	*−0.9*	**−3.1**	*−0.4*
$-\left\langle \omega \frac{\partial m}{\partial p} \right\rangle$	**−9.1**	**−3.2**	**−7.5**	**−11.4**	**−10.8**	**−7.3**	**−9.7**	**−8.4**
$-\left\langle \omega \frac{\partial \overline{\overline{m}}}{\partial p} \right\rangle$	**−13.8**	**−12.4**	**−22.6**	**−30.6**	**−19.8**	**−10.8**	**−18.1**	**−15.1**
$-\left\langle \omega \frac{\partial \overline{m}(x)}{\partial p} \right\rangle$	**2.5**	**2.8**	**4.4**	**5.6**	**4.0**	**1.9**	**3.4**	**3.5**
$-\left\langle \omega \frac{\partial m'(x,t)}{\partial p} \right\rangle$	**2.2**	**6.4**	**10.7**	**13.6**	**5.1**	**1.6**	**5.0**	**3.3**
$\langle Q_R \rangle$	**1.6**	**5.5**	**12.1**	**14.3**	**4.3**	**1.2**	**5.8**	**2.6**
$H + LE$	**1.2**	*0.9*	**2.8**	**2.5**	**−2.4**	**0.8**	**−0.7**	**−2.1**
Residual	*−1.9*	*−1.1*	**−1.2**	**−1.3**	*0.0*	*−1.2*	**1.0**	*−0.4*

results with ERAI radiative heating (Fig. 6) are approximately in quantitative agreement with more direct estimates (Fig. 8 of Adames and Kim 2016) for low-wavenumber and low-frequency disturbances, although *P*-correlated cloudy radiation anomalies appear to be underanalyzed at smaller scales in the ERAI forecast tendencies dataset, as described in section 3d.

Larger residuals of the imaginary or quadrature component indicate that only a few terms can be considered robust, especially horizontal advection for the

TABLE 2. As in Table 1, but for the imaginary component of the cross-spectrum.

	WIGn1	TD	ERn1	MJO	Klvn	WIGn2	MRG	EIGn0
$\left\langle \frac{\partial m}{\partial t} \right\rangle$	**11.3**	**40.5**	**22.4**	**12.1**	**11.3**	**11.2**	**20.8**	**12.7**
$\langle -\mathbf{v}_h \cdot \nabla_h m \rangle$	*0.8*	**39.1**	**17.2**	**13.2**	*1.2*	*1.0*	**3.4**	*0.8*
$-\langle \mathbf{v}_h \cdot \nabla_h \overline{m}(x) \rangle$	**−1.3**	**−7.2**	**−11.9**	**4.9**	*−0.6*	**−0.9**	**−3.4**	*−0.8*
$-\langle \mathbf{v}_h \cdot \nabla_h m'(x,t) \rangle$	*2.1*	**46.4**	**29.1**	**8.3**	*1.8*	*1.8*	**6.7**	*1.6*
$-\left\langle \omega \frac{\partial m}{\partial p} \right\rangle$	**5.6**	**1.7**	**2.2**	**−0.9**	**4.3**	**6.5**	**10.2**	**8.3**
$-\left\langle \omega \frac{\partial \overline{\overline{m}}}{\partial p} \right\rangle$	**5.8**	**3.2**	**2.1**	**−2.0**	**5.6**	**6.7**	**10.4**	**9.2**
$-\left\langle \omega \frac{\partial \overline{m}(x)}{\partial p} \right\rangle$	**1.0**	*−0.3*	**0.3**	**1.9**	**1.1**	**0.8**	**2.0**	**1.5**
$-\left\langle \omega \frac{\partial m'(x,t)}{\partial p} \right\rangle$	**−1.2**	**−1.2**	*−0.1*	**−0.9**	**−2.4**	**−1.0**	**−2.2**	**−2.4**
$\langle Q_R \rangle$	**−1.7**	**−1.3**	**−0.3**	**−2.9**	**−3.9**	**−1.5**	**−3.2**	**−2.6**
$H + LE$	*0.1*	**−1.4**	**4.0**	**−4.1**	**1.1**	*−0.1*	**3.0**	*−0.4*
Residual	**6.6**	**2.4**	**−0.8**	**6.9**	**8.6**	**5.3**	**7.5**	**6.5**

MJO and ERn1 wave disturbances, which has a role in leading these disturbances (13.2% and 17.2%, respectively). Decomposition indicates that horizontal advection of *time-mean* MSE would tend to lead to both MJO and ERn1 wave disturbances to the eastward direction, while horizontal advection of the remainder drives them in different directions (eastward and westward, respectively). The importance of such anomalous eddy components includes any rectified effects of synoptic substructure, as well as the disturbance-scale correlations of flow and moisture, so further decomposition would be required to test whether synoptic eddies may be important to eastward and westward propagations of these planetary-scale MSE + precipitation disturbances (e.g., Maloney and Dickinson 2003; Sobel and Maloney 2012).

The importance of coupling between atmosphere and ocean is a longtime question regarding the destablization of intraseasonal time-scale disturbances (DeMott et al. 2015), the most familiar hypothesis being wind-induced surface heat exchange (WISHE; Emanuel 1987; Neelin et al. 1987). It is widely accepted that coupling improves the fidelity of intraseasonal variations in a model (e.g., Flatau et al. 1997; Waliser et al. 1999; Woolnough et al. 2001; Kemball-Cook et al. 2002; Inness and Slingo 2003; Maloney and Sobel 2004; and many others). On the other hand, recent idealized models suggest that air–sea coupling is not an essential process (e.g., Raymond 2001; Wang and Liu 2011; Sobel and Maloney 2012; Thual et al. 2014; Adames and Kim 2016). Our estimates here support the idea that surface heat flux is of secondary importance to the amplification of MJO, although it is sometimes significant locally (e.g., Dellaripa and Maloney 2015). However, the results here also suggest that surface flux on the west might be important in slowing MJO propagation, an effect emphasized in some early MJO studies (reviewed in Zhang 2005), since its effect on the westward propagation is largest for the MJO (−4.1%), which is at least comparable to the large residuals (6.9%).

b. *Kelvin wave and inertia–gravity (EIGn0, WIGn1, and WIGn2) wave disturbances*

The Kelvin and EIGn0 wave filter regions are slightly amplified by radiation (4.3% and 2.6% of latent heat release, respectively), while they are significantly damped by vertical advection (−10.8% and −8.4%, respectively) and more weakly by surface heat flux (−2.4% and −2.1%, respectively) and horizontal advection (−2.0% and −1.0%, respectively). Similar features are found in the WIGn1 and WIGn2 wave disturbances (amplification through the radiation process, 1.6% and 1.2%, respectively, and damping through vertical advection, −9.1% and −7.3%, respectively), although the effect of the surface heat flux is opposite (1.2% and 0.8%, respectively) and horizontal advection acts to more significantly damp the disturbances (−4.9% and −2.6%, respectively). Decomposition indicates that the vertical advective damping is enhanced with the tropical mean MSE and that the amplification effect of the nonlinear positive feedback between moisture and vertical motion is more than twice as big as that of radiation processes (the wave-scale MSE anomaly by the background vertical wind is also included in the "nonlinear positive feedback").

These divergent wave disturbances also share similar characteristics in the imaginary (propagation) component: They are led by vertical advection and retarded by radiation. Compared with the more horizontally advected types of disturbance (MJO, ERn1, and TD-type modes), one remarkable feature is that vertical advection dominates the contribution of the other propagation terms (4.3%, 8.3%, 5.6%, and 6.5% for Kelvin, EIGn0, WIGn1, and WIGn2 wave disturbances, respectively), which can be mostly accounted for by wave-scale self-advection of time–space-mean MSE. However, large residual imaginary components (8.6%, 6.5%, 6.6%, and 5.3% for Kelvin, EIGn0, WIGn1, and WIGn2 wave disturbances) caution against too quantitative a conclusion from these data.

c. *TD-type and MRG wave disturbances*

Transition from MRG wave disturbances to off-equatorial TD-type disturbances is reported by previous works (e.g., Takayabu and Nitta 1993; Dunkerton and Baldwin 1995; Dickinson and Molinari 2002). The similarity and difference of the cross-spectrum between the two disturbances is, therefore, worth special consideration.

The CMSE anomalies associated with TD-type and MRG filter regions are mildly amplified by radiation (5.5% and 5.8% of latent heat release, respectively), while they are damped by vertical advection (−3.2% and −9.7%, respectively) and effects of the surface heat flux are modest (0.9% and −0.7%, respectively). TD-type disturbances show the weakest damping effect of vertical advection among all types of disturbance. Horizontal advection plays a distinctly different role: It amplifies the TD-type disturbance (5.5%), while the MRG wave disturbance is weakly damped (−0.6%). Decomposition indicates that horizontal advection of the time-mean pattern of MSE plays a role in amplifying the MRG wave disturbance and damping the TD-type mode, respectively, an oblique glimpse of the consequences of their longitude-dependent occurrence patterns. Horizontal advection of remainders from the time-mean MSE is a significant damping for MRG wave disturbances but amplifies the TD-type mode. Further

decomposition into mean-flow, wave-scale self-advection, and subwave-scale rectification would be needed to further interpret this difference.

In terms of the propagation (imaginary component), the TD-type and MRG wave disturbances are predominantly led by horizontal (39.1%) and vertical advections (10.2%), respectively. The MRG wave disturbance shares similar characteristics to the gravity wave family of disturbances (led by vertical advection), but leading effects of horizontal advection and surface heat flux are also relatively large. On the other hand, the TD-type disturbance is unique, since horizontal advection can exclusively account for the leading effect. Perhaps in the transition of MRG wave disturbances to TD-type disturbances, the dominant driving force for propagation shifts from vertical advection to horizontal advection, which might be one of the essential features that distinguishes between dynamical and nondynamical modes.

6. Concluding remarks

In the present study, budgets of CMSE were analyzed in zonal wavenumber–frequency space, making use of satellite-derived precipitation to isolate correlated aspects of ERAI reanalysis data. The evolution of CMSE has previously been regressed against (or composited around) filtered precipitation series associated with a particular type of the disturbance to reveal the relative importance of each term in CMSE budget equation to the charging and discharging mechanisms of CMSE. Here we extended that approach to the entire subseasonal spectral domain, utilizing the cross-spectrum between precipitation and each term in MSE budget equation. We believe that this framework can be useful to grasp the different CMSE budget characteristics of different CCEWs at a glance. Despite the elimination of P in CMES budgets [Eq. (3)], this approach connects indirectly to the daydream (or lofty goal) of "precipitation budgets," as the strong WTG approximation links CMSE to CWV, which is monotonically, if nonlinearly, related to the statistical expectation of precipitation.

If model-forecasted precipitation or column-integrated vertical advection of DSE were used as a measure of convective activity instead of TRMM precipitation, all terms in Eqs. (4) or (5) could be calculated from model outputs only. Indeed, model CMSE itself could be used and the result would simply be its variance budget in the model. However, even state-of-the-art models, and their associated assimilated reanalyses, suffer from biases, especially in moist processes (e.g., Mapes and Bacmeister 2012; Yokoi 2015), so such a study might emphasize artificial characteristics. For this reason, we chose our approach of using almost-independent TRMM-3B42 data. The projection to the more directly observed precipitation is one of the main advantages of the present study.

To explain some essential features of the MJO and CCEWs, theoretical works generally examine necessary conditions for small perturbations to exponentially amplify, assuming a sinusoidal solution in a linearized equation for moisture or MSE or similar variables (e.g., Neelin and Yu 1994; Raymond 2000, 2001; Sobel et al. 2001; Fuchs and Raymond 2002, 2005, 2007; Sobel and Bretherton 2003; Raymond and Fuchs 2007; Sobel and Maloney 2012, 2013; Adames and Kim 2016; and many others). For such an unstable solution to emerge in the model, phase relationships of the perturbation with various terms included in the prognostic equation are the key. The cross-spectrum gives directly useful empirical estimates of these phase differences over a wide range of wavenumbers and frequency and could be a powerful tool for targeting theoretical framings to the phenomena they are meant to elucidate. With this connection to basic understanding, it is hoped that the work reported here may serve as both a data resource and a methodological inspiration for additional observational studies.

Acknowledgments. The results in the present study were obtained using TRMM-3B42 and ERA-Interim. We would like to express our sincere thanks to all concerned in these products. This work was supported by JSPS KAKENHI Grant Numbers JP25400463, JP16KK0095, JP16K05560, and JP16H04048. BEM acknowledges support from NASA Grant NNX15AD11G. Scientific discussions with Drs. George Kiladis, Juliana Dias, and Stefan Tulich and helpful comments from Drs. Tomoki Miyakawa, Noriyuki Nishi, Ángel F. Adames, and an anonymous reviewer are gratefully acknowledged.

APPENDIX

Interpretations of Real and Imaginary Components of the Cross-Spectrum

Under the WTG approximation, the column-integrated evolution of MSE is equivalent to the evolution of CWV. Namely, $\langle \partial m/\partial t \rangle \approx L(\partial/\partial t)\langle q \rangle$ and Eq. (3) can be rewritten as

$$L\frac{\partial}{\partial t}\langle q\rangle' = -\langle \mathbf{v}_h \cdot \nabla_h m\rangle' - \omega\left\langle \frac{\partial m}{\partial p}\right\rangle' + \langle Q_R\rangle' + (H + LE)', \tag{A1}$$

where the prime indicates a departure from the time average. We assume that the precipitation anomaly P' has a form of

$$P' = \hat{P}\exp(\omega_r t + i\omega_i t),$$

where $\hat{P}$ is an amplitude ($\hat{P} > 0$), and ω_r, and ω_i are real and imaginary components of frequency, respectively (we can set $\omega_i > 0$ without loss of generality). We further assume that all terms in Eq. (A1) coherently vary with the precipitation anomaly and can be expressed as

$$Lq' = \widehat{A_q} \exp(\omega_r t + i\omega_i t + i\theta_q),$$

$$-\langle \mathbf{v}_h \cdot \nabla_h m \rangle' = \widehat{A_h} \exp(\omega_r t + i\omega_i t + i\theta_h),$$

$$-\omega \frac{\partial m'}{\partial p} = \widehat{A_v} \exp(\omega_r t + i\omega_i t + i\theta_v), \quad \text{and}$$

$$Q'_R + (H + LE)' = \widehat{F_s} \exp(\omega_r t + i\omega_i t + i\theta_s),$$

where $\widehat{A_q}$, $\widehat{A_h}$, $\widehat{A_v}$, and $\widehat{F_s}$ are amplitudes ($\widehat{A_q}$, $\widehat{A_h}$, $\widehat{A_v}$, $\widehat{F_s} > 0$), and θ_q, θ_h, θ_v, and θ_s are phase differences ($-180° \le \theta_q$, θ_h, θ_v, $\theta_s < 180°$). It should be noted that a minus sign is included in advection terms to make the discussion easier, which is usually excluded from the definition of GMS. Plugging these into Eq. (A1) yields

$$\begin{aligned} &\widehat{A_q}\,\omega_r \exp(\omega_r t + i\omega_i t + i\theta_q) + i\omega_i \widehat{A_q}(t) \exp(\omega_r t + i\omega_i t + i\theta_q) \\ &\quad = \widehat{A_h} \exp(\omega_r t + i\omega_i t + i\theta_h) + \widehat{A_v} \exp(\omega_r t + i\omega_i t + i\theta_v) \\ &\qquad + \widehat{F_s} \exp(\omega_r t + i\omega_i t + i\theta_s). \end{aligned} \tag{A2}$$

If the CWV anomaly *simultaneously* varies with the precipitation anomaly, $\theta_q = 0$. Then, multiplication of the complex conjugate of precipitation anomaly to Eq. (A2) yields

$$\omega_r \widehat{A_q} + i\omega_i \widehat{A_q} = \widehat{A_h} \exp(i\theta_h) + \widehat{A_v} \exp(i\theta_v) + \widehat{F_s} \exp(i\theta_s). \tag{A3}$$

Real and imaginary components of Eq. (A3) are

$$\omega_r \widehat{A_q} = \widehat{A_h} \cos\theta_h + \widehat{A_v} \cos\theta_v + \widehat{F_s} \cos\theta_s, \quad \text{and}$$

$$\omega_i \widehat{A_q} = \widehat{A_h} \sin\theta_h + \widehat{A_v} \sin\theta_v + \widehat{F_s} \sin\theta_s.$$

In the spectral analysis, of course, the amplitude is assumed to be constant in a long enough time series, and the total of real terms on the RHS equals 0 (i.e., $\omega_r = 0$). However, on a term-by-term basis, we can say that positive real values of terms on the RHS act to amplify disturbances of that frequency and wavenumber, while negative values act to damp them. Likewise, the positive or negative phase difference can be evaluated by a sign of the imaginary component, and we may say that a positive (negative) value of the imaginary part of any term on the RHS acts to advance (retard) the phase of a disturbance.

REFERENCES

Adames, Á. F., 2017: Precipitation budget of the Madden–Julian oscillation. *J. Atmos. Sci.*, **74**, 1799–1817, https://doi.org/10.1175/JAS-D-16-0242.1.

——, and D. Kim, 2016: The MJO as a dispersive, convectively coupled moisture wave: Theory and observations. *J. Atmos. Sci.*, **73**, 913–941, https://doi.org/10.1175/JAS-D-15-0170.1; Corrigendum, **74**, 3121–3124, https://doi.org/10.1175/JAS-D-17-0071.1.

Andersen, J. A., and Z. Kuang, 2012: Moist static energy budget of MJO-like disturbances in the atmosphere of a zonally symmetric aquaplanet. *J. Climate*, **25**, 2782–2804, https://doi.org/10.1175/JCLI-D-11-00168.1.

Bantzer, C. H., and J. M. Wallace, 1996: Intraseasonal variability in tropical mean temperature and precipitation and their relation to the tropical 40–50 day oscillation. *J. Atmos. Sci.*, **53**, 3032–3045, https://doi.org/10.1175/1520-0469(1996)053<3032:IVITMT>2.0.CO;2.

Bellenger, H., K. Yoneyama, M. Katsumata, T. Nishizawa, K. Yasunaga, and R. Shirooka, 2015: Observation of moisture tendencies related to shallow convection. *J. Atmos. Sci.*, **72**, 641–659, https://doi.org/10.1175/JAS-D-14-0042.1.

Benedict, J. J., E. D. Maloney, A. H. Sobel, and D. M. W. Frierson, 2014: Gross moist stability and MJO simulation skill in three full-physics GCMs. *J. Atmos. Sci.*, **71**, 3327–3349, https://doi.org/10.1175/JAS-D-13-0240.1.

Berrisford, P., and Coauthors 2011: The ERA-Interim archive version 2.0. European Centre for Medium-Range Weather Forecasts ERA Rep., 23 pp., https://www.ecmwf.int/sites/default/files/elibrary/2011/8174-era-interim-archive-version-20.pdf.

Bony, S., and K. A. Emanuel, 2005: On the role of moist processes in tropical intraseasonal variability: Cloud–radiation and moisture–convection feedbacks. *J. Atmos. Sci.*, **62**, 2770–2789, https://doi.org/10.1175/JAS3506.1.

Bretherton, C. S., and A. H. Sobel, 2002: A simple model of a convectively coupled Walker circulation using the weak temperature gradient approximation. *J. Climate*, **15**, 2907–2920, https://doi.org/10.1175/1520-0442(2002)015<2907:ASMOAC>2.0.CO;2.

——, M. E. Peters, and L. E. Back, 2004: Relationships between water vapor path and precipitation over the tropical oceans. *J. Climate*, **17**, 1517–1528, https://doi.org/10.1175/1520-0442(2004)017<1517:RBWVPA>2.0.CO;2.

Burpee, R. W., 1972: The origin and structure of easterly waves in the lower troposphere of North Africa. *J. Atmos. Sci.*, **29**, 77–90, https://doi.org/10.1175/1520-0469(1972)029<0077:TOASOE>2.0.CO;2.

——, 1974: Characteristics of north African easterly waves during the summers of 1968 and 1969. *J. Atmos. Sci.*, **31**, 1556–1570, https://doi.org/10.1175/1520-0469(1974)031<1556:CONAEW>2.0.CO;2.

——, 1975: Some features of synoptic–scale waves based on a compositing analysis of GATE data. *Mon. Wea. Rev.*, **103**, 921–925, https://doi.org/10.1175/1520-0493(1975)103<0921:SFOSWB>2.0.CO;2.

Carlson, T. N., 1969: Synoptic histories of three African disturbances that developed into Atlantic hurricanes. *Mon. Wea. Rev.*, **97**, 256–276, https://doi.org/10.1175/1520-0493(1969)097<0256:SHOTAD>2.3.CO;2.

Charney, J. G., 1963: A note on large-scale motions in the tropics. *J. Atmos. Sci.*, **20**, 607–609, https://doi.org/10.1175/1520-0469(1963)020<0607:ANOLSM>2.0.CO;2.

Dellaripa, E. M. R., and E. D. Maloney, 2015: Analysis of MJO wind-flux feedbacks in the Indian Ocean using RAMA buoy observations. *J. Meteor. Soc. Japan*, **93A**, 1–20, https://doi.org/10.2151/jmsj.2015-021.

DeMott, C. A., N. P. Klingaman, and S. J. Woolnough, 2015: Atmosphere-ocean coupled processes in the Madden-Julian oscillation. *Rev. Geophys.*, **53**, 1099–1154, https://doi.org/10.1002/2014RG000478.

Dickinson, M., and J. Molinari, 2002: Mixed Rossby–gravity waves and western Pacific tropical cyclogenesis. Part I: Synoptic evolution. *J. Atmos. Sci.*, **59**, 2183–2196, https://doi.org/10.1175/1520-0469(2002)059<2183:MRGWAW>2.0.CO;2.

Dunkerton, T. J., and M. P. Baldwin, 1995: Observation of 3–6-day meridional wind oscillations over the tropical Pacific, 1973–1992: Horizontal structure and propagation. *J. Atmos. Sci.*, **52**, 1585–1601, https://doi.org/10.1175/1520-0469(1995)052<1585:OODMWO>2.0.CO;2.

Emanuel, K. A., 1987: An air–sea interaction model of intraseasonal oscillations in the tropics. *J. Atmos. Sci.*, **44**, 2324–2340, https://doi.org/10.1175/1520-0469(1987)044<2324:AASIMO>2.0.CO;2.

Flatau, M., P. J. Flatau, P. Phoebus, and P. P. Niiler, 1997: The feedback between equatorial convection and local radiative and evaporative processes: The implications for intraseasonal oscillations. *J. Atmos. Sci.*, **54**, 2373–2386, https://doi.org/10.1175/1520-0469(1997)054<2373:TFBECA>2.0.CO;2.

Frank, N. L., 1969: The ''inverted V'' cloud pattern—An easterly wave? *Mon. Wea. Rev.*, **97**, 130–140, https://doi.org/10.1175/1520-0493(1969)097<0130:TVCPEW>2.3.CO;2.

Fuchs, Ž., and D. J. Raymond, 2002: Large-scale modes of a nonrotating atmosphere with water vapor and cloud–radiation feedbacks. *J. Atmos. Sci.*, **59**, 1669–1679, https://doi.org/10.1175/1520-0469(2002)059<1669:LSMOAN>2.0.CO;2.

——, and ——, 2005: Large-scale modes in a rotating atmosphere with radiative–convective instability and WISHE. *J. Atmos. Sci.*, **62**, 4084–4094, https://doi.org/10.1175/JAS3582.1.

——, and ——, 2007: A simple, vertically resolved model of tropical disturbances with a humidity closure. *Tellus*, **59A**, 344–354, https://doi.org/10.1111/j.1600-0870.2007.00230.x.

Gill, A. E., 1980: Some simple solutions for heat-induced tropical circulation. *Quart. J. Roy. Meteor. Soc.*, **106**, 447–462, https://doi.org/10.1002/qj.49710644905.

Hall, N. M. J., G. N. Kiladis, and C. D. Thorncroft, 2006: Three-dimensional structure and dynamics of African easterly waves. Part II: Dynamical modes. *J. Atmos. Sci.*, **63**, 2231–2245, https://doi.org/10.1175/JAS3742.1.

Hannah, W. M., and E. D. Maloney, 2014: The moist static energy budget in NCAR CAM5 hindcasts during DYNAMO. *J. Adv. Model. Earth Syst.*, **6**, 420–440, https://doi.org/10.1002/2013MS000272.

Hayashi, Y., 1974: Spectral analysis of tropical disturbances appearing in a GFDL general circulation model. *J. Atmos. Sci.*, **31**, 180–218, https://doi.org/10.1175/1520-0469(1974)031<0180:SAOTDA>2.0.CO;2.

Hendon, H. H., and M. C. Wheeler, 2008: Some space–time spectral analyses of tropical convection and planetary-scale waves. *J. Atmos. Sci.*, **65**, 2936–2948, https://doi.org/10.1175/2008JAS2675.1.

Hirota, I., M. Shiotani, T. Sakurai, and J. C. Glue, 1991: Kelvin waves near the equatorial stratopause as seen in SBUV ozone data. *J. Meteor. Soc. Japan*, **69**, 179–186, https://doi.org/10.2151/jmsj1965.69.2_179.

Hitchman, M. H., and C. B. Leovy, 1988: Estimation of the Kelvin wave contribution to the semiannual oscillation. *J. Atmos. Sci.*, **45**, 1462–1475, https://doi.org/10.1175/1520-0469(1988)045<1462:EOTKWC>2.0.CO;2.

Huffman, G. J., and Coauthors, 2007: The TRMM Multisatellite Precipitation Analysis (TMPA): Quasi-global, multiyear, combined-sensor precipitation estimates at fine scales. *J. Hydrometeor.*, **8**, 38–55, https://doi.org/10.1175/JHM560.1.

Inness, P. M., and J. M. Slingo, 2003: Simulation of the Madden–Julian oscillation in a coupled general circulation model. Part I: Comparison with observations and an atmosphere-only GCM. *J. Climate*, **16**, 345–364, https://doi.org/10.1175/1520-0442(2003)016<0345:SOTMJO>2.0.CO;2.

Inoue, K., and L. E. Back, 2015a: Column-integrated moist static energy budget analysis on various time scales during TOGA COARE. *J. Atmos. Sci.*, **72**, 1856–1871, https://doi.org/10.1175/JAS-D-14-0249.1.

——, and ——, 2015b: Gross moist stability assessment during TOGA COARE: Various interpretations of gross moist stability. *J. Atmos. Sci.*, **72**, 4148–4166, https://doi.org/10.1175/JAS-D-15-0092.1.

——, and ——, 2017: Gross moist stability analysis: Assessment of satellite-based products in the GMS plane. *J. Atmos. Sci.*, **74**, 1819–1837, https://doi.org/10.1175/JAS-D-16-0218.1.

Itoh, H., 1977: The response of equatorial waves to thermal forcing. *J. Meteor. Soc. Japan*, **55**, 222–239, https://doi.org/10.2151/jmsj1965.55.3_222.

Johnson, R. H., T. M. Rickenbach, S. A. Rutledge, P. E. Ciesielski, and W. H. Schubert, 1999: Trimodal characteristics of tropical convection. *J. Climate*, **12**, 2397–2418, https://doi.org/10.1175/1520-0442(1999)012<2397:TCOTC>2.0.CO;2.

Kemball-Cook, S., B. Wang, and X. Fu, 2002: Simulation of the intraseasonal oscillation in the ECHAM-4 model: The impact of coupling with an ocean model. *J. Atmos. Sci.*, **59**, 1433–1453, https://doi.org/10.1175/1520-0469(2002)059<1433:SOTIOI>2.0.CO;2.

Kikuchi, K., and Y. N. Takayabu, 2003: Equatorial circumnavigation of moisture signal associated with the Madden-Julian oscillation (MJO) during boreal winter. *J. Meteor. Soc. Japan*, **81**, 851–869, https://doi.org/10.2151/jmsj.81.851.

Kiladis, G. N., and K. M. Weickmann, 1992: Circulation anomalies associated with tropical convection during northern winter. *Mon. Wea. Rev.*, **120**, 1900–1923, https://doi.org/10.1175/1520-0493(1992)120<1900:CAAWTC>2.0.CO;2.

——, M. C. Wheeler, P. T. Haertel, K. H. Straub, and P. E. Roundy, 2009: Convectively coupled equatorial waves. *Rev. Geophys.*, **47**, RG2003, https://doi.org/10.1029/2008RG000266; Corrigendum, **49**, RG3004, https://doi.org/10.1029/2011RG000370.

Kim, D., M.-S. Ahn, I.-S. Kang, and A. D. Del Genio, 2015: Role of longwave cloud–radiation feedback in the simulation of the Madden–Julian oscillation. *J. Climate*, **28**, 6979–6994, https://doi.org/10.1175/JCLI-D-14-00767.1.

King, M. J., M. C. Wheeler, and T. P. Lane, 2015: Association of convection with the 5-day Rossby–Haurwitz wave. *J. Atmos. Sci.*, **72**, 3309–3321, https://doi.org/10.1175/JAS-D-14-0316.1.

——, ——, and ——, 2017: Mechanisms linking global 5-day waves to tropical convection. *J. Atmos. Sci.*, **74**, 3679–3702, https://doi.org/10.1175/JAS-D-17-0101.1.

Kiranmayi, L., and E. D. Maloney, 2011: Intraseasonal moist static energy budget in reanalysis data. *J. Geophys. Res.*, **116**, D21117, https://doi.org/10.1029/2011JD016031.

Kohyama, T., and J. M. Wallace, 2016: Rainfall variations induced by the lunar gravitational atmospheric tide and their implications for the relationship between tropical rainfall and humidity. *Geophys. Res. Lett.*, **43**, 918–923, https://doi.org/10.1002/2015GL067342.

Kuang, Z., 2008: A moisture-stratiform instability for convectively coupled waves. *J. Atmos. Sci.*, **65**, 834–854, https://doi.org/10.1175/2007JAS2444.1; Corrigendum, **65**, 3011, https://doi.org/10.1175/2008JAS2844.1.

Liebmann, B., and H. H. Hendon, 1990: Synoptic-scale disturbances near the equator. *J. Atmos. Sci.*, **47**, 1463–1479, https://doi.org/10.1175/1520-0469(1990)047<1463:SSDNTE>2.0.CO;2; Corrigendum, **47**, 2035, https://doi.org/10.1175/1520-0469(1990)047<2035:C>2.0.CO;2.

Lin, J.-L., and B. E. Mapes, 2004: Radiation budget of the tropical intraseasonal oscillation. *J. Atmos. Sci.*, **61**, 2050–2062, https://doi.org/10.1175/1520-0469(2004)061<2050:RBOTTI>2.0.CO;2.

Ma, D., and Z. Kuang, 2011: Modulation of radiative heating by the Madden-Julian oscillation and convectively coupled Kelvin waves as observed by CloudSat. *Geophys. Res. Lett.*, **38**, L21813, https://doi.org/10.1029/2011GL049734.

Madden, R. A., and P. R. Julian, 1971: Detection of a 40–50 day oscillation in the zonal wind in the tropical Pacific. *J. Atmos. Sci.*, **28**, 702–708, https://doi.org/10.1175/1520-0469(1971)028<0702:DOADOI>2.0.CO;2.

——, and ——, 1972: Description of global-scale circulation cells in the tropics with a 40–50 day period. *J. Atmos. Sci.*, **29**, 1109–1123, https://doi.org/10.1175/1520-0469(1972)029<1109:DOGSCC>2.0.CO;2.

Maloney, E. D., and D. L. Hartmann, 2001: The Madden–Julian oscillation, barotropic dynamics, and North Pacific tropical cyclone formation. Part I: Observations. *J. Atmos. Sci.*, **58**, 2545–2558, https://doi.org/10.1175/1520-0469(2001)058<2545:TMJOBD>2.0.CO;2.

——, and M. J. Dickinson, 2003: The intraseasonal oscillation and the energetics of summertime tropical western North Pacific synoptic-scale disturbances. *J. Atmos. Sci.*, **60**, 2153–2168, https://doi.org/10.1175/1520-0469(2003)060<2153:TIOATE>2.0.CO;2.

——, and A. H. Sobel, 2004: Surface fluxes and ocean coupling in the tropical intraseasonal oscillation. *J. Climate*, **17**, 4368–4386, https://doi.org/10.1175/JCLI-3212.1.

Mapes, B. E., and J. T. Bacmeister, 2012: Diagnosis of tropical biases and the MJO from patterns in the MERRA analysis tendency fields. *J. Climate*, **25**, 6202–6214, https://doi.org/10.1175/JCLI-D-11-00424.1.

——, S. Tulich, J. Lin, and P. Zuidema, 2006: The mesoscale convection life cycle: Building block or prototype for large-scale tropical waves? *Dyn. Atmos. Oceans*, **42**, 3–29, https://doi.org/10.1016/j.dynatmoce.2006.03.003.

——, E. S. Chung, W. M. Hannah, H. Masunaga, A. J. Wimmers, and C. S. Velden, 2018: The meandering margin of the meteorological moist tropics. *Geophys. Res. Lett.*, **45**, 1177–1184, https://doi.org/10.1002/2017GL076440.

Masunaga, H., and T. S. L'Ecuyer, 2014: A mechanism of tropical convection inferred from observed variability in the moist static energy budget. *J. Atmos. Sci.*, **71**, 3747–3766, https://doi.org/10.1175/JAS-D-14-0015.1.

Matsuno, T., 1966: Quasi-geostrophic motions in the equatorial area. *J. Meteor. Soc. Japan*, **44**, 25–43, https://doi.org/10.2151/jmsj1965.44.1_25.

Matthews, A. J., and R. A. Madden, 2000: Observed propagation and structure of the 33-h atmospheric Kelvin wave. *J. Atmos. Sci.*, **57**, 3488–3497, https://doi.org/10.1175/1520-0469(2000)057<3488:OPASOT>2.0.CO;2.

Milliff, R. F., and R. A. Madden, 1996: The existence and vertical structure of fast, eastward-moving disturbances in the equatorial troposphere. *J. Atmos. Sci.*, **53**, 586–597, https://doi.org/10.1175/1520-0469(1996)053<0586:TEAVSO>2.0.CO;2.

Neelin, J. D., and I. M. Held, 1987: Modeling tropical convergence based on the moist static energy budget. *Mon. Wea. Rev.*, **115**, 3–12, https://doi.org/10.1175/1520-0493(1987)115<0003:MTCBOT>2.0.CO;2.

——, and J.-Y. Yu, 1994: Modes of tropical variability under convective adjustment and the Madden–Julian oscillation. Part I: Analytical theory. *J. Atmos. Sci.*, **51**, 1876–1894, https://doi.org/10.1175/1520-0469(1994)051<1876:MOTVUC>2.0.CO;2.

——, I. M. Held, and K. H. Cook, 1987: Evaporation-wind feedback and low-frequency variability in the tropical atmosphere. *J. Atmos. Sci.*, **44**, 2341–2348, https://doi.org/10.1175/1520-0469(1987)044<2341:EWFALF>2.0.CO;2.

——, O. Peters, and K. Hales, 2009: The transition to strong convection. *J. Atmos. Sci.*, **66**, 2367–2384, https://doi.org/10.1175/2009JAS2962.1.

Nitta, T., 1970: Statistical study of tropospheric wave disturbances in the tropical Pacific region. *J. Meteor. Soc. Japan*, **48**, 47–60, https://doi.org/10.2151/jmsj1965.48.1_47.

——, 1978: A diagnostic study of interaction of cumulus updrafts and downdrafts with large-scale motions in GATE. *J. Meteor. Soc. Japan*, **56**, 232–242, https://doi.org/10.2151/jmsj1965.56.4_232.

——, and Y. Takayabu, 1985: Global analysis of the lower tropospheric disturbances in the tropics during the northern summer of the FGGE year part II: Regional characteristics of the disturbances. *Pure Appl. Geophys.*, **123**, 272–292, https://doi.org/10.1007/BF00877023.

Raymond, D. J., 2000: Thermodynamic control of tropical rainfall. *Quart. J. Roy. Meteor. Soc.*, **126**, 889–898, https://doi.org/10.1002/qj.49712656406.

——, 2001: A new model of the Madden–Julian oscillation. *J. Atmos. Sci.*, **58**, 2807–2819, https://doi.org/10.1175/1520-0469(2001)058<2807:ANMOTM>2.0.CO;2.

——, and Ž. Fuchs, 2007: Convectively coupled gravity and moisture modes in a simple atmospheric model. *Tellus*, **59**, 627–640, https://doi.org/10.1111/j.1600-0870.2007.00268.x.

——, S. L. Sessions, A. H. Sobel, and Ž. Fuchs, 2009: The mechanics of gross moist stability. *J. Adv. Model. Earth Syst.*, **1**, 9, https://doi.org/10.3894/JAMES.2009.1.9.

Reed, R. J., and E. E. Recker, 1971: Structure and properties of synoptic-scale wave disturbances in the equatorial western Pacific. *J. Atmos. Sci.*, **28**, 1117–1133, https://doi.org/10.1175/1520-0469(1971)028<1117:SAPOSS>2.0.CO;2.

——, D. C. Norquist, and E. E. Recker, 1977: The structure and properties of African wave disturbances as observed during phase III of GATE. *Mon. Wea. Rev.*, **105**, 317–333, https://doi.org/10.1175/1520-0493(1977)105<0317:TSAPOA>2.0.CO;2.

Rushley, S. S., D. Kim, C. S. Bretherton, and M.-S. Ahn, 2018: Reexamining the nonlinear moisture-precipitation relationship over the tropical oceans. *Geophys. Res. Lett.*, **45**, 1133–1140, https://doi.org/10.1002/2017GL076296.

Sakaeda, N., and P. E. Roundy, 2016: Gross moist stability and the Madden–Julian oscillation in reanalysis data. *Quart. J. Roy. Meteor. Soc.*, **142**, 2740–2757, https://doi.org/10.1002/qj.2865.

Sakazaki, T., K. Hamilton, C. Zhang, and Y. Wang, 2017: Is there a stratospheric pacemaker controlling the daily cycle of tropical rainfall? *Geophys. Res. Lett.*, **44**, 1998–2006, https://doi.org/10.1002/2017GL072549.

Salby, M. L., D. L. Hartmann, P. L. Bailey, and J. C. Gille, 1984: Evidence for equatorial Kelvin modes in Nimbus-7 LIMS. *J. Atmos. Sci.*, **41**, 220–235, https://doi.org/10.1175/1520-0469(1984)041<0220:EFEKMI>2.0.CO;2.

Schiro, K. A., J. D. Neelin, D. K. Adams, and B. R. Lintner, 2016: Deep convection and column water vapor over tropical land versus tropical ocean: A comparison between the Amazon and the tropical western Pacific. *J. Atmos. Sci.*, **73**, 4043–4063, https://doi.org/10.1175/JAS-D-16-0119.1.

Schultz, D. M., P. N. Schumacher, and C. A. Doswell III, 2000: The intricacies of instabilities. *Mon. Wea. Rev.*, **128**, 4143–4148, https://doi.org/10.1175/1520-0493(2000)129<4143:TIOI>2.0.CO;2.

Sherwood, S. C., 2000: On moist instability. *Mon. Wea. Rev.*, **128**, 4139–4142, https://doi.org/10.1175/1520-0493(2000)129<4139:OMI>2.0.CO;2.

Sobel, A. H., and C. S. Bretherton, 1999: Development of synoptic-scale disturbances over the summertime tropical northwest Pacific. *J. Atmos. Sci.*, **56**, 3106–3127, https://doi.org/10.1175/1520-0469(1999)056<3106:DOSSDO>2.0.CO;2.

——, and ——, 2003: Large-scale waves interacting with deep convection in idealized mesoscale model simulations. *Tellus*, **55**, 45–60, https://doi.org/10.3402/tellusa.v55i1.12084.

——, and H. Gildor, 2003: A simple time-dependent model of SST hot spots. *J. Climate*, **16**, 3978–3992, https://doi.org/10.1175/1520-0442(2003)016<3978:ASTMOS>2.0.CO;2.

——, and E. Maloney, 2012: An idealized semi-empirical framework for modeling the Madden–Julian oscillation. *J. Atmos. Sci.*, **69**, 1691–1705, https://doi.org/10.1175/JAS-D-11-0118.1.

——, and ——, 2013: Moisture modes and the eastward propagation of the MJO. *J. Atmos. Sci.*, **70**, 187–192, https://doi.org/10.1175/JAS-D-12-0189.1.

——, J. Nilsson, and L. M. Polvani, 2001: The weak temperature gradient approximation and balanced tropical moisture waves. *J. Atmos. Sci.*, **58**, 3650–3665, https://doi.org/10.1175/1520-0469(2001)058<3650:TWTGAA>2.0.CO;2.

——, S. Wang, and D. Kim, 2014: Moist static energy budget of the MJO during DYNAMO. *J. Atmos. Sci.*, **71**, 4276–4291, https://doi.org/10.1175/JAS-D-14-0052.1.

Sumi, Y., and H. Masunaga, 2016: A moist static energy budget analysis of quasi-2-day waves using satellite and reanalysis data. *J. Atmos. Sci.*, **73**, 743–759, https://doi.org/10.1175/JAS-D-15-0098.1.

Takayabu, Y. N., and M. Murakami, 1991: The structure of super cloud clusters observed in 1-20 June 1986 and their relationship to easterly waves. *J. Meteor. Soc. Japan*, **69**, 105–125, https://doi.org/10.2151/jmsj1965.69.1_105.

——, and T. Nitta, 1993: 3-5 day-period disturbances coupled with convection over the tropical Pacific Ocean. *J. Meteor. Soc. Japan*, **71**, 221–246, https://doi.org/10.2151/jmsj1965.71.2_221.

Thorncroft, C. D., and B. J. Hoskins, 1994: An idealized study of African easterly waves. I: A linear view. *Quart. J. Roy. Meteor. Soc.*, **120**, 953–982, https://doi.org/10.1002/qj.49712051809.

Thual, S., A. J. Majda, and S. N. Stechmann, 2014: A stochastic skeleton model for the MJO. *J. Atmos. Sci.*, **71**, 697–715, https://doi.org/10.1175/JAS-D-13-0186.1.

Tian, B., and V. Ramanathan, 2003: A simple moist tropical atmosphere model: The role of cloud radiative forcing. *J. Climate*, **16**, 2086–2092, https://doi.org/10.1175/1520-0442(2003)016<2086:ASMTAM>2.0.CO;2.

Waliser, D. E., K. M. Lau, and J.-H. Kim, 1999: The influence of coupled sea surface temperatures on the Madden–Julian oscillation: A model perturbation experiment. *J. Atmos. Sci.*, **56**, 333–358, https://doi.org/10.1175/1520-0469(1999)056<0333:TIOCSS>2.0.CO;2.

Wallace, J. M., 1971: Spectral studies of tropospheric wave disturbances in the tropical western Pacific. *Rev. Geophys.*, **9**, 557–612, https://doi.org/10.1029/RG009i003p00557.

Wang, B., and F. Liu, 2011: A model for scale interaction in the Madden–Julian oscillation. *J. Atmos. Sci.*, **68**, 2524–2536, https://doi.org/10.1175/2011JAS3660.1.

Wheeler, M., and G. N. Kiladis, 1999: Convectively coupled equatorial waves: Analysis of clouds and temperature in the wavenumber–frequency domain. *J. Atmos. Sci.*, **56**, 374–399, https://doi.org/10.1175/1520-0469(1999)056<0374:CCEWAO>2.0.CO;2.

——, ——, and P. J. Webster, 2000: Large-scale dynamical fields associated with convectively coupled equatorial waves. *J. Atmos. Sci.*, **57**, 613–640, https://doi.org/10.1175/1520-0469(2000)057<0613:LSDFAW>2.0.CO;2.

Woolnough, S. J., J. M. Slingo, and B. J. Hoskins, 2001: The organization of tropical convection by intraseasonal sea surface temperature anomalies. *Quart. J. Roy. Meteor. Soc.*, **127**, 887–907, https://doi.org/10.1002/qj.49712757310.

Yanai, M., S. Esbensen, and J.-H. Chu, 1973: Determination of bulk properties of tropical cloud clusters from large-scale heat and moisture budgets. *J. Atmos. Sci.*, **30**, 611–627, https://doi.org/10.1175/1520-0469(1973)030<0611:DOBPOT>2.0.CO;2.

Yasunaga, K., and B. Mapes, 2012: Differences between more divergent and more rotational types of convectively coupled equatorial waves. Part I: Space–time spectral analyses. *J. Atmos. Sci.*, **69**, 3–16, https://doi.org/10.1175/JAS-D-11-033.1.

——, and ——, 2014: Differences between faster versus slower components of convectively coupled equatorial waves. *J. Atmos. Sci.*, **71**, 98–111, https://doi.org/10.1175/JAS-D-13-03.1.

——, K. Yoneyama, Q. Moteki, M. Fujita, Y. N. Takayabu, J. Suzuki, T. Ushiyama, and B. Mapes, 2010: Characteristics of 3–4- and 6–8-day period disturbances observed over the tropical Indian Ocean. *Mon. Wea. Rev.*, **138**, 4158–4174, https://doi.org/10.1175/2010MWR3469.1.

——, T. Nasuno, H. Miura, Y. N. Takayabu, and M. Yoshizaki, 2013: Afternoon precipitation peak simulated in an aqua-planet global non-hydrostatic model (aqua-planet-NICAM). *J. Meteor. Soc. Japan*, **91A**, 217–229, https://doi.org/10.2151/jmsj.2013-A07.

Yokoi, S., 2015: Multireanalysis comparison of variability in column water vapor and its analysis increment associated with the Madden–Julian oscillation. *J. Climate*, **28**, 793–808, https://doi.org/10.1175/JCLI-D-14-00465.1.

——, and A. H. Sobel, 2015: Intraseasonal variability and seasonal march of the moist static energy budget over the eastern Maritime Continent during CINDY2011/DYNAMO. *J. Meteor. Soc. Japan*, **93A**, 81–100, https://doi.org/10.2151/jmsj.2015-041.

Zhang, C., 2005: Madden–Julian oscillation. *Rev. Geophys.*, **43**, RG2003, https://doi.org/10.1029/2004RG000158.

Zurovac-Jevtić, D., S. Bony, and K. Emanuel, 2006: On the role of clouds and moisture in tropical waves: A two-dimensional model study. *J. Atmos. Sci.*, **63**, 2140–2155, https://doi.org/10.1175/JAS3738.1.